Department of Nanoscopy, Istituto Italiano di Tecnologia, Genova, Italy

DIFILab, Università degli studi di Genova, Genova, Italy

A thesis submitted for the degree of

Doctor of Philosophy

NANOSCALE INVESTIGATION OF CHROMATIN ORGANIZATION BY STRUCTURED ILLUMINATION MICROSCOPY

Isotta Cainero

Ph.D. supervisors:

Prof. Luca Lanzanò

Prof. Alberto Diaspro

Ph.D. course in Physics

XXXIII Cycle

…To my family

"You are the wind beneath my wings"

Bette Midler

Table of Contents

Abstract

This thesis work aims to present a novel approach to reconstruct Structured Illumination Microscopy, SIM, raw data and to analyze SIM reconstructed images. These new approaches will be demonstrated in the study of chromatin organization.

The dissertation will be articulated as follows:

Chapter 1 provides an introduction to chromatin nanoscale organization and optical fluorescence microscopy, which is one of the main tools involved in life sciences studies. Indeed, optical microscopy allowed investigating, with high specificity and sensitivity, living samples such as cells, and even tissues. The reader will be presented with a summary on the fluorescence optical microscopy and on the super-resolution, SR, techniques available today including SIM, which is the microscope used in this thesis work.

In **Chapter 2** the focus is on the introduction of a new reconstruction tool for specific SR-SIM microscopy powered by the Separation of Photons by Lifetime Tuning, SPLIT, method. The introduction of the concept, applied in other works to different SR techniques, will be followed by the practical implementation of the method on the SIM microscope. Then, the applicability of the technique, which we called SPLIT-SIM, will be demonstrated on several different samples. Indeed, it will be used on Simulated data, on test experimental beads, on biological samples both in one and two-color staining.

In **Chapter 3** the focus will move on the coupling of SIM reconstructed data to colocalization analysis. In particular, for the first time, SIM was coupled to Image Cross-Correlation Spectroscopy, ICCS, in the study of two-color images of a model sample. DNA origami-based structures were chosen as a model sample with precise distances allowing for evaluation of the analysis results. Moreover, all the images analyzed by the pixel-based technique, SIM-ICCS, were analyzed also with an object-based technique as a comparison to evaluate which could be the best choice in SIM acquisitions.

Finally, **Chapter 4** will be focused on the application of the analysis, performed in chapter 3, to two-color SIM images of nuclear structure. The analysis will be performed on ‘positive control’ in which the target structures will be colocalized and on a negative control in which the structured are spatially segregated within the nucleus. Both object-based and pixel-based analysis will be able to extract coherent results thus showing how SIM-ICCS can become an interesting and useful tool to analyze SIM multicolor acquisitions.

CHAPTER 1

Introduction

Chromatin Organization at the nanoscale

Despite its discovery almost 130 years ago, the hierarchical nanoscale organization of Chromatin within cell nuclei remains still unclear [1]. In eukaryotic cells, chromatin 3D dynamic organization is fundamental to modulate all biological processes. It is organized in high-order structure starting from the sequences -histones complex to chromosome territories. The basic structures of chromatin are the nucleosomes. These are protein octamers organized with a core, composed of two copies of H3-H4 histones, two copies of H2A-H2B histones, and with the N-terminal tails of the nucleosome projecting outward [2,3]. Each core is wrapped 1,7 times by 147 base-pair DNA. At the beginning and the end of these 147bp, there are 10-80bp of DNA bound to the linker histone, H1, which role is to stabilize chromatin subunit structure [4]. These nucleosomes, organized by DNAlinker-H1 complex, form a 10nm fiber structure which looks like a 'beads on a string' structure, in which the beads are the nucleosomes and the string is the DNA strand [5]. In vitro, it has been shown that the 10nm fiber forms a 30nm helical fiber [6]. In this higher-order organization, there are 6-11 nucleosome-octamers per turn [7]. In vivo, there is little evidence of this 30nm fiber structure, and it has been proposed that sample preparation methods can favor the formation of this structure in vitro [8]. Even with a complex structure, Chromatin-DNA and histones are very dynamic. Nucleosome tails are subjected to post-translational modifications (PTMs) which are enzymatic activities fundamental as signaling pathways [9,10]. These PTMs, such as methylation, acetylation, sumoylation, phosphorylation, and citrullination modify chromatin organization defining its function [11,12,]. For example, methylation of Lysine 4 in Histone H3 is a sign of active transcription, whereas it is a sign of strong silencing if it occurs on H3K27 by Polycomb groups. PTMs are fundamental in chromatin organization, dynamics, and transcriptional regulation, but they have also been involved with some diseases such as cancer, autoimmune disorders, and also neurological diseases. [13].

Chromatin organization also depends on the activity of Architectural chromatin proteins which appear to be responsible for long-range chromatin interactions [14].

However, the primary order folding of chromatin, which consists of nucleosomes octamers, are three-dimensionally organized in a higher-order folding, secondary chromatin structure, depending on the degree of compaction needed [15]. Interactions between the secondary structure of chromatin cause the formation of a more complex higher-order folding that is the tertiary chromatin structure, corresponding to chromosomes.

During the cell cycle, chromosomes undergo a dramatic structural change passing from mitosis to interphase. During interphase, it has been shown that they are non-randomly organized as Chromosome Territories (CTs) and usually the localization of some chromosomes is maintained, not only from parent cells to daughter, but also throughout evolution [16].

As shown in figure 1.1, in the interphase nuclei Chromosome territories are composed of two types of chromatin depending on its compaction and localization. *Euchromatin* is considered as the 'active chromatin', rich in genes and characterized by less compaction. It is generally located in the central region of the nuclei and is usually referred as the 10nm fiber 'beads on a string' structure. On the other hand, *heterochromatin* is the 'inactive chromatin' that is highly compacted and has been described as the 30nm fiber. Heterochromatin is located in the nuclear and nucleolar periphery and is divided into facultative and constitutive heterochromatin. Facultative heterochromatin consists of transcriptionally silenced regions that can loosen their compaction to allow transcription during the cell cycle or developmental stages [17]. Constitutive heterochromatin is characterized by high copy numbers of tandem repeats, corresponding to 6.5% of the genome. Constitutive heterochromatin is characterized by methylation of the Lysin 9 in Histone H3 (meH3K9). This methylation is a binding site for Heterochromatin Protein 1 (HP1) which has also the role to recruit proteins involved in chromatin compaction [18].

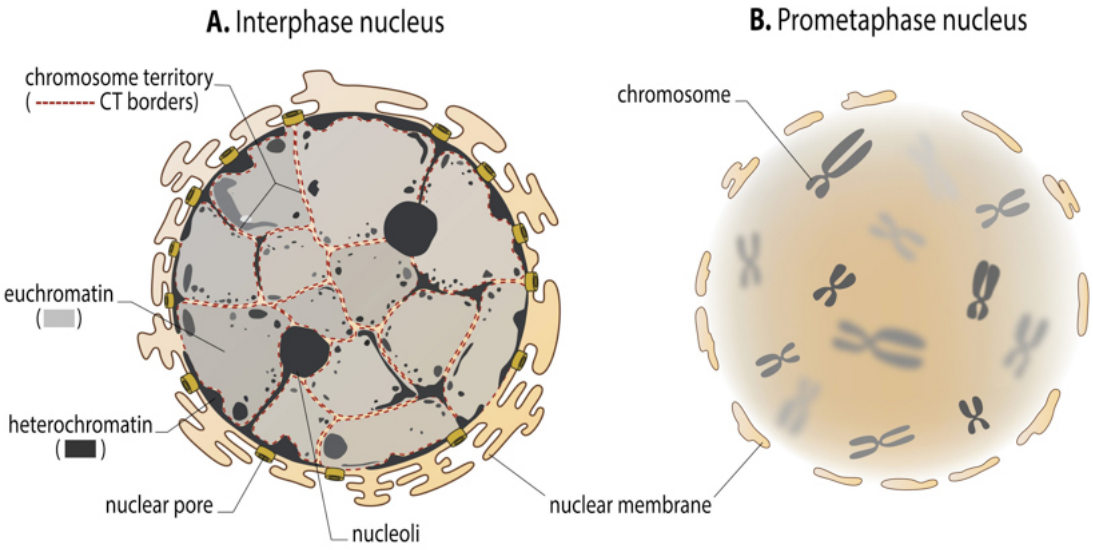

Figure 1.1 Euchromatin and Heterochromatin. **a)** Interphase nucleus in which chromosome are not easily distinguishable, but they occupy chromosome territories, in the figure are delimited by red dashed lines. Euchromatin, transcriptionally active, is in light grey whilst heterochromatin, transcriptionally silent, is in dark grey. **b)** during cell division, chromosomes can be easily distinguished. (image credit mechanobio.info)

Modernly it is widely accepted that the modulation of chromatin organization is fundamental in regulating the expression of genes involved in cellular processes such as transcription, replication, and DNA damage response (DDR). These cellular functions need precise coordination of each cellular machinery. For example, the promotion of transcription needs a morphological modification of chromatin organization which is performed by chromatin remodeling complexes. Indeed, their role is to increase the accessibility of nucleosomal DNA to transcriptional factors (TFs) thus chromatin remodeling complexes cause the formation of DNA loop due to a temporary unwrapping of DNA around the nucleosome core, or due to the sliding of a nucleosome from its original location to another transcriptional position [19]. Another fundamental cellular process that requires dynamic ongoing of the DNA-chromatin complex is the replication of DNA sequence. An immediate consequence of this process is the dissolution and then reassembly of chromatin structure due to replication fork formation. When replication occurs, the DNA double strand, dsDNA, needs to be open so that one strand can be used as a primer to synthesize the second strand. Indeed, the histone octamers-DNA interaction needs to be disrupted ahead of the replication fork.

The parental histones will be recycled and used behind the fork while newly synthesized histones will be deposed onto the nascent dsDNA. These two processes of disrupting and deposing parental and new histones octamers is crucial in defining the inheritance of chromatin states and genome stability [20]. Another fundamental process for the life of a cell is the ability to repair eventual damages to the dsDNA, the so-called DNA Damage Response (DDR). This process comprehends both concentration of DNA-repair proteins in the site of the damage, but also post-translational modification of nucleosomes to loosen or tighten the closer region to allow accessibility for the DNA-repair proteins. There are multiple options in the DDR response depending on the type of DNA break, but in all cases the process is divided into three main steps. The first step is Damage recognition, performed by several different proteins depending on the DNA damage itself, followed by the rearrangement of histones and DNA interacting protein to allow accessibility of DNA-repair protein into the site of the damage. The third steps consist of the repair synthesis of new DNA, then the restoration of the original local chromatin architecture and the removal of the DNA-repair protein. Thus, it is clear how important is the role of modulations in chromatin architecture to allow all these three processes introduced above, DNA damage recognition, DNA repair and repair synthesis of new DNA [21]. Each of these three processes; transcription, replication, and DNA damage repair, are crucial in the integrity maintenance of the genomic functions, and to avoid the onset of mutations that could give rise to cancer development or diseases. Additionally, any problem in chromatin organization and maintenance could generate further complications leading to pathological development.

In the 1990s many techniques were developed to study the relationship between chromatin functions and their organization. Genomic techniques provided information about a cell developmental stages, genetic mutations, and characterization of genomes, thus reaching a very specific spatio-temporal information about the regulation and epigenetic expression of every gene [22, 23]. All these techniques, however, lack single-cell resolution and spatial distribution within intact cell nuclei. The first microscopy techniques able to study the ultrastructure of chromatin, pushing the resolution down to the nanoscale, was Electron Microscopy (EM) [24]. Indeed, in the late 20th

century, EM allowed the in-situ visualization of nucleosomes thanks to a Feulgen-like reaction using osmium-ammine staining of DNA [25,26]. This particular staining is characterized by very high resolution in thin sections, allowing the visualization of 2-3nm DNA filaments and nucleosomes. This particular staining revealed a 11nm structure whose dimension strongly suggested the measuring of nucleosomes. Thus, early EM experiments have shown that the basic unit of chromatin was the nucleosome core defining the ‘beads on a string’ structure [27].

The introduction of another technique, cryogenic Electron Microscopy (cryo-EM) was crucial in the study of molecular structures. It is based on a particular sample preparation method, invented by Dubochet and coworkers [28], and it consists of keeping samples preserved within a thin ice film and observing it with a low-dose transmission Electron Microscopy, TEM. Together with cryo-EM, X-ray crystallography and nuclear magnetic resonance (NMR) spectroscopy became the most powerful tools to investigate biological molecule's structures with a near-atomic resolution. Since its introduction, cryo-EM [29] was able to map the 3D structure of chromatin and the visualization, in-situ, of 10nm fibers even in a compact environment such as heterochromatin [30,31]. A new revolutionary technique to study chromatin organization was made by Ou et al in 2017 [32]. They developed a DNA-staining method, ChromEM, able to reveal the ultrastructure and the 3D organization of chromatin polymers, megabase domains, and also mitotic chromosomes in situ. ChromEM is used with the TEM to resolve structures down to 1.6nm. With this technique, they demonstrated that chromatin is a disordered chain, 5 to 24nm diameter, and it seems that it is not organized as the classical high order folding description [32]. These EM methods were crucial in these discoveries, but they do not have molecular specificity and, due to their invasiveness, they cannot be applied to living samples. However, the main limiting factor of these techniques is that they cannot be used in living cells, due to the sample preparation protocols. To perform traditional Electron Microscopy measurements, the specimen needs to be chemically fixed, then dehydrated, embedded in plastic polymers, dissected, stained, and then visualized under the electron microscope [33,34]. Instead, to perform cryo-EM measurements, the sample needs to be cryo-immobilized, then it needs to be

subjected to freeze substitution, which is a process of dehydration of the sample carried out at a low temperature to avoid ice crystal formation, then the sample is embedded in plastic before finally being dissected, stained and visualized [35]. Traditional TEM protocol procedures are very invasive and the dehydration of the sample can give rise to questions, such as the reliability of the final images compared to hydrated samples. Notably, Cryo-EM does not require the dehydration of the sample. But, due to the low temperatures required, it is not suitable for living specimens. Almost all these limitations can be avoided using optical microscopy. In this context, light microscopy became very useful in the 20th century in providing specific information about cellular structures, cellular molecules, and also about DNA and chromatin organization. The specificity and contrast achievable in optical microscopy are due to the use of fluorescent probes with a high affinity to target molecules. The resolution of optical microscopy was constrained to the Abbe diffraction limit (i.e. ~250nm) until the advent of super-resolution techniques, starting from the last decade of the twentieth century. Thanks to super-resolution microscopy (SRM) techniques it is possible to probe single molecules achieving a spatial resolution even smaller than 50nm [36]. This, in addition to molecule specificity, makes SRM a great technique to investigate nanoscale chromatin interaction and organization.

SRM techniques are widely used to investigate chromatin organization, including Stochastic optical reconstruction microscopy (STORM) [37,38,39], Photo-activated localization microscopy (PALM) [40], STimulated Emission Depletion microscopy (STED) [41], and Structured Illumination Microscopy (SIM) [42,43]. Depending on the experiment that needs to be performed, it is possible to couple SRM with multiple techniques such as fluorescence recovery after photobleaching (FRAP), an example is single-molecule coupled with FRAP, or Fluorescence lifetime imaging microscopy (FLIM) and Fluorescence correlation spectroscopy (FCS), but the description of these techniques is beyond the purpose of this thesis.

Fluorescence Optical Microscopy

Since its discovery, fluorescence became a fundamental tool in the examination of biological samples. Fluorescence-based techniques helped in answering fundamental questions in biomedical and biological sciences. And allowed the study of biological samples with different techniques, e.g. proteomics, bioengineering, genomics, medical diagnosis, microbiology, and biophysics. In these techniques, fluorescence can be used as substrates for enzymes, as ion indicators, and as molecular labels [44,45]. Fluorophores, i.e. fluorescent molecules, can be sorted into two main classes: intrinsic and extrinsic. Intrinsic fluorophores are naturally present in a living being and includes chlorophyll, aromatic amino acids, NADH, or fluorescent proteins. While extrinsic fluorophores are synthetic and generally used to stain non-fluorescent samples. Fluorescence protein cannot be included in the description above, in fact, these particular proteins are used to genetically mutate organisms, making them produce genetically modified proteins.

Nowadays there are a large number of fluorophores and fluorescence techniques which give the possibility to address the same question in multiple ways. For this thesis, I will focus my attention only on the used fluorophores: conjugated fluorophores and fluorescent stains. To label specific molecules within intact cells, fluorophores are conjugated to carriers to facilitate their penetration inside the sample and to confine fluorophores in a specific area of the sample. The most common technique is immunofluorescence, which exploits immunoglobulins as carriers for the fluorophores. Immunostaining is broadly used because of the high affinity of an immunoglobulin to stain a specific target protein, giving not only the fluorescence in the sample but also fluorescence-specificity. The most popular immunofluorescence technique is ‘indirect’ immunofluorescence, in which the non-fluorescent primary antibody is probing the target molecule, whilst the fluorescent-conjugated secondary antibody links to the primary antibody. These techniques have an increased signal due to the link of the multiple secondary antibodies to the primary ones. There is also experimental flexibility, thanks to the wide range of commercial fluorophores [46]. The high specificity, the contrast enhancement, and the non-

toxicity given by fluorophores, in respect to other invasive techniques such as electron microscopy, make them the perfect choice for optical microscopy.

In optical microscopy, the emitted light of a sub-diffraction point-like source will always pass through a finite circular aperture of the objective, called numerical aperture (NA), so it will always be subjected to the diffraction limit. The resulting diffraction pattern of the point-like source is called an Airy Disk and is characterized by a bright region in the center with a series of concentric rings around, as shown in figure 1.2. The Airy disk is also a description of the Point Spread Function (PSF) of a microscope, which is how a point-like source will be seen by the imaging system. The PSF is a function that defines the resolving power of a microscope. The PSF represents the intensity distribution of the point-like source in the lateral (x,y) and axial (z) dimensions, and its x,y area is strictly linked to the wavelength (λ) of the illuminating light and the size of the numerical aperture of the objective. The x,y,z distribution of the PSF curve, provides a value of the spatial resolution through the measurements of the Full-Width Half Maximum (FWHM) of the curve. The PSF and the Abbe diffraction law limit the resolution of a traditional optical microscope to the 250-200nm maximum. This means that when two or more molecules are closer than 200nm they will not be resolved by the microscope and will be considered as one.

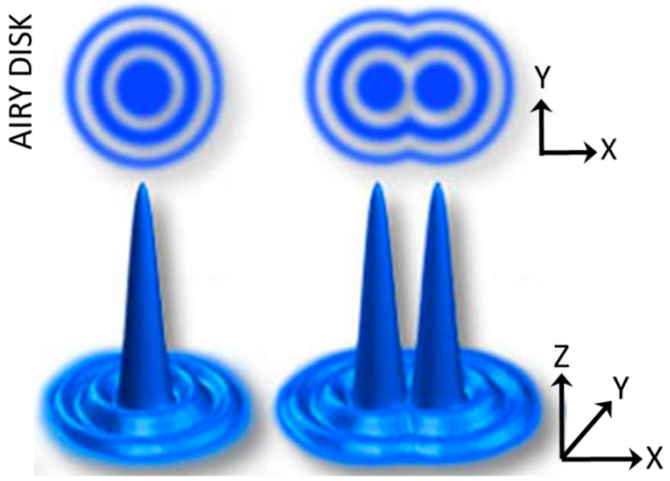

Figure 1.2. Airy disk diffraction pattern. Illustration of the intensity distribution of the Airy disk, which correspond to the PSF, in the lateral (**x**,**y**) dimensions.

(Image adapted from Olympus-lifescience.com)

The diffraction limit of a microscope was defined by Ernst Abbe in 1873 [47].

$$d = \frac{\lambda}{2NA}$$

In the formula, *d* is the resolvable feature size, is the wavelength used, and NA is the numerical aperture of the objective lens.

$$NA = nsin\alpha$$

NA is defined as the refraction index of the medium, n, multiplicated with sinα, which is the half-angle subtended by the objective. To define the axial resolution, the three-dimensional diffraction pattern of the point-like source is usually considered, and is defined as the minimum distance of diffraction points along the axial direction [48,49]. In traditional optical microscopy, the axial resolution is ~500nm, lower than the lateral one.

Super-resolution microscopy breaks the diffraction limit

Traditional optical fluorescence microscopy proved to be a fundamental tool to investigate biological samples due to its non-invasiveness, specificity, and multicolor imaging thanks to the wide variety of fluorescent labels and fluorescent proteins. Despite all these advantages, optical microscopy does not have enough resolving power to study biological processes and interactions which occur in the range of just a few nanometers. In the last decades, many implementations in optical fluorescence microscopy allowed to overcome the limit of diffraction reaching nanometer resolution [50]. Thanks to super-resolution techniques it is finally possible to investigate biological samples at the molecular level, visualizing the interaction of individual molecules within intact living cells [51].

The possibility to overcome the diffraction limit was demonstrated, among others, by Betzig, Hell, and Moerner, Nobel laureates in Chemistry in 2014 [54, 55]. The diffraction barrier can be circumvented by using particular fluorophores, which can be selectively switched ‘on’ and ‘off’. This ‘trick’ allows differentiating between very close fluorophores by avoiding the collection of concurrent emissions.

Several techniques have been introduced since then, extending the resolution power down to a few nanometers. SR Methods are based on widefield (WF), confocal, and total internal reflection fluorescence (TIRF) microscope setups. Even if they are based on different setups, they all rely on the switching or the modulation of fluorophore emissions. Depending on how fluorophores are handled, SR techniques can be divided into two main groups. The first one comprehends Single Molecule Localization Microscopy (SMLM). These techniques are based on widefield illumination and rely on single molecule imaging utilizing stochastic switching of the fluorophores. For this reason, this group is also referred as 'stochastic switching techniques. This group includes, for instance, photoactivation localization microscope (PALM) and stochastic optical reconstruction microscopy (STORM) [52,53]. The second group is based on confocal setups and makes use of focused laser beams to perform the 'on/off' switching of the fluorophores. It is also known as the group of 'targeted switching' techniques. This group comprehends Stimulated Emission Depletion (STED), Saturated Structured Illumination Microscopy (SSIM) and REversible Saturable OpticaL Fluorescence Transitions, RESOLFT [54,55]. Many of these techniques have been involved in studies concerning the nuclear environment and chromatin organization at the nanoscale within intact cell nuclei.

Stochastic switching Super Resolution techniques

The 'stochastic switching' group, comprehends Single Molecule Localization Microscopy, SMLM. Single molecule techniques achieve sub-diffraction resolution images by implementing a widefield microscope. Indeed, in SMLM the widefield excitation is performed with a high-power laser and the detection is done by using a charge-coupled device, a CCD camera. The laser stochastically activates only a few molecules of the sample at a time and the intensity peak of the image produced by each molecule can be used to localize precisely the position of the molecule. Every emitted photon is detected by the CCD camera and the molecule's position is given by the calculation of the centroid of the fluorescent signal. The precision in defining the centroid position mainly depends on the photon counts. to reconstruct a SR image, thousands of frames need to be acquired. To perform this type of

measurements, traditional fluorophores are not suitable. Indeed, there have been introduced photo-switchable dyes, whose fluorescence emission can be controlled and only a subset of probes at a time will be activated. When the dyes are excited by the laser, only a small random fraction of these fluorophores will be activated and then switched off into a reversible dark state or for photobleached, thus will not emit fluorescence. This continuous repetition of turning 'on and off' allows the acquisition thousands of frames in which different particles are excited, accumulating information about the distributions of each single molecule in the sample. Thus multiple acquisitions are used to map every particle position attributing x,y,z information to each single molecule as shown in figure 1.3. From the SMLM principle, several techniques have been introduced such as Photo-activated localization microscopy (PALM) and Stochastic optical reconstruction microscopy (STORM). The resolution achievable with these techniques in the x,y focal plane reaches ~20-30nm. The increasing interest in studying biological samples in their three-dimensional shapes, led the implementation of SMLM to the 3D imaging. Thanks to the use of astigmatic lenses, Zhuang et al reached an axial resolution of ~50-60nm [56].

SMLM techniques have been applied in the study of chromatin organization reaching an incredible resolution. In 2010 Matsuda et al. used PALM and EGFP to study chromosome structure during mitosis [40], in 2012 Zessin et al. used STORM to image chromosomal DNA [37], in 2015 Ricci et al reached almost 20nm resolution imaging chromatin structure by probing histones H2B [38]. Prakash et al implied the photoconversion of DNA-dyes to study meiotic chromosomes in mouse oocytes [57]. In 2017 Nozaki and collaborators performed measurements on dynamic chromatin structures in living Hela cells, by using PALM coupled with single nucleosome tracking linked to photo-switchable mCherry histone H2B [58].

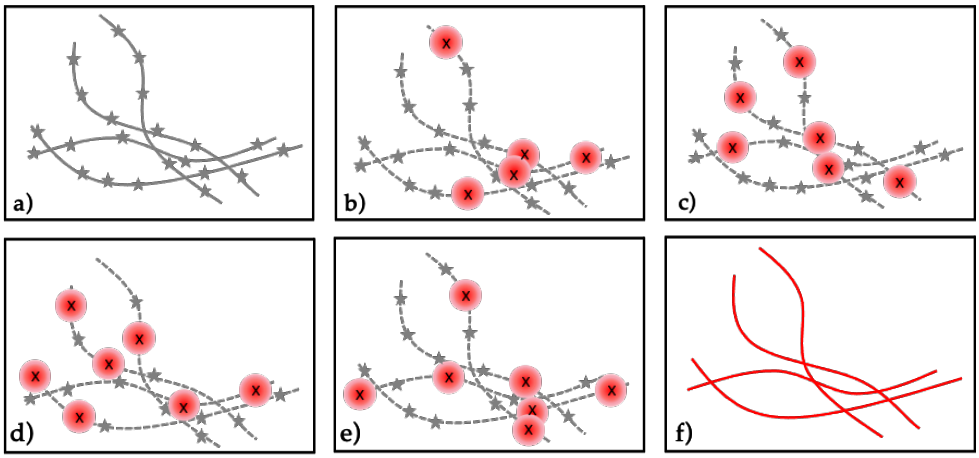

Figure 1.3 Basic principle of STORM imaging. a) schematic of stained microtubules in a cell. **b)** Strong laser excitation induces most fluorophores to a dark state, from which some single fluorophores may stochastically return to an emissive state (red cirles), each centroid position is identified (black crosses), and then mapped in a single super-resolution reconstruction **(f)**. **c-e)** Single emitters are recorded over a large number of frames.

Targeted switching Super Resolution techniques

The second group of SR techniques comprehends the targeted switching techniques in which fluorophore emission is influenced by a spatially shaped illumination. Among these techniques, we will only cite STED microscopy

Stimulated Emission Depletion Microscopy

Stimulated Emission Depletion Microscopy was developed by Hell and his colleagues at the beginning of the 1990s'. With this technique they were able to break the diffraction limit, thus opening the possibility to image cellular processes and molecules at the nanoscale. In this technique, schematized in figure 1.4, the first laser excites the fluorophores within the PSF, then an additional doughnut shaped laser is superimposed on the excitation beam. This doughnut laser depletes the invested fluorophores in the periphery of the PSF, through stimulated emission, allowing the emission only from the fluorophores located in the center of the PSF. The depletion beam can switch 'off' the fluorophore because of its red-shift wavelength and its high power [54]. Indeed, the FWHM of the PSF of a STED system decreases by increasing the STED laser power. Therefore, the superimposition of two different lasers gives

the possibility of reaching super-resolution imaging of sub-cellular molecules and interactions.

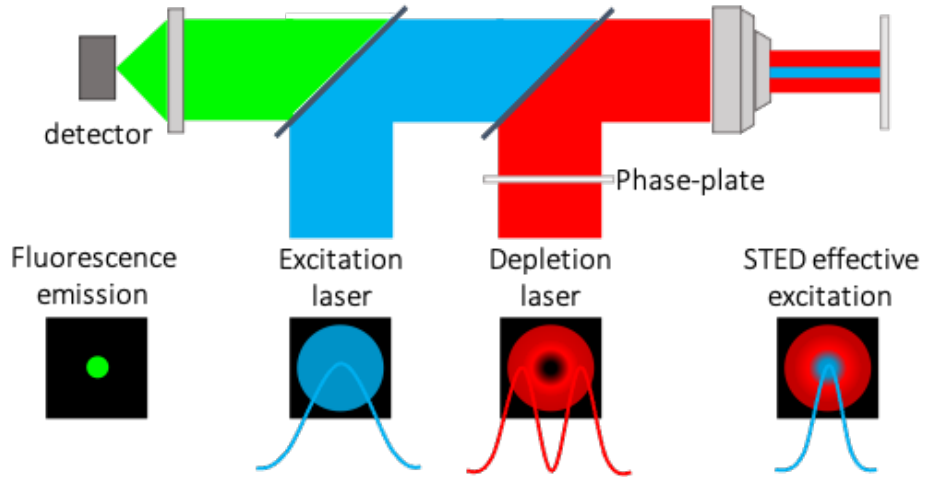

Figure 1.4 Scheme of basic STED setup. The excitation laser and the STED beam, in light blue and red respectively, are merged at a dichroic mirror. Thanks to a phase-plate, the STED beam is shaped into a 'doughnut'. The excitation light is allowed to excite fluorophores everywhere in the excitation volume, while the STED laser will deplete the emission of fluorophores in the peripheral region. The signal is then detected by a point detector.

In theory, by increasing the depletion power, STED resolution is unlimited thus reaching molecular dimensions. Unfortunately, increasing the laser power leads to the decrease of the Signal to Noise Ratio (SNR), creating noisy images in which the resolution is decreased. Another reason why STED cannot reach molecular sizes is that the increase of the power could cause fluorophores photobleaching, or even destroy biological samples due to laser heating. Since its introduction, there have been many developments in the engineering of fluorophores and advances in STED techniques, but we will focus only on one particular implementation which is Separation of Photons by lifetime tuning (SPLIT).

The SPLIT approach is based on a simple concept, shown in figure 1.5. To extract sub-diffraction information from a STED observation volume, let's assume that the center and the periphery of the PSF can be separated in two different regions in respect to a parameter. If so, with SPLIT, it is possible to discriminate these two regions through an additional parameter, thus separate them in a central region, used to create the final image, and in a peripheral one that won't contribute to the information needed for the SR image.

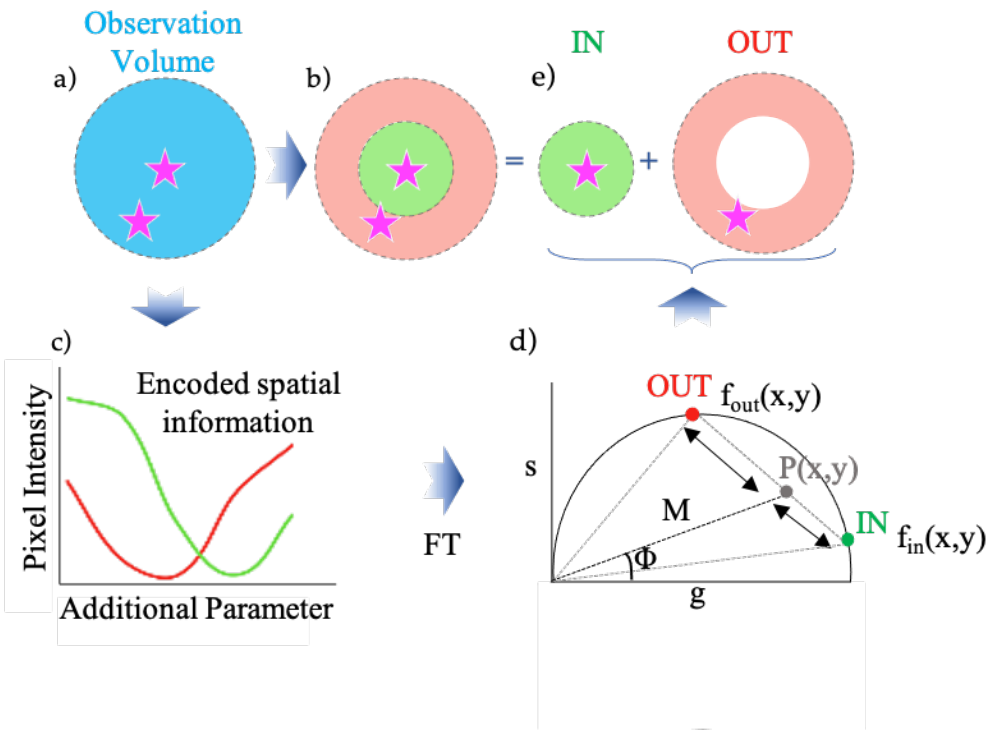

Figure 1.5 Schematic of SPLIT principle. a) Fluorophores, pink stars, randomly sparse in a Diffraction limited PSF. **b-c)** If their position can be discriminated through an additional parameter, then, d) it is possible to discriminate their location by using the phasor plot and **e)** separate them to reconstruct the final image 'IN' by discarding the information coming from the periphery of the PSF, 'OUT'.

In continuous wave, CW, STED it has been proven that the 'in and out' areas can be separated by using as an additional parameter, the fluorescence lifetime. Indeed, the application of a higher power laser in the periphery shortens the lifetime of the fluorophores located in the doughnut area. Whilst the lifetime of the fluorophore located in the center will not be affected by the depletion laser. To perform SPLIT-STED it is fundamental to implement the setup by adding a Time-correlated single-photon counting (TCSPC) module to record the lifetimes.

Lifetime-based SPLIT-STED allows separating the photons coming from the central area of the PSF, characterized by a longer lifetime, from the photons coming from the outer area of the PSF, whose lifetime has been shortened by the STED depletion beam [59].

The SPLIT method was also coupled with STED microscopy using another 'additional parameter', demonstrating how versatile this algorithm could be.

Indeed, in 2017, Sarmento and collaborators showed how it is possible to use the tunability of the laser power as parameter to perform super-resolution SPLIT-STED measurements. In their work, they demonstrated that tuning the laser power of the STED beam induces spatially encoded variations of the fluorescence emission which can be extracted from the analysis of the phasor plot [60].

Like SMLM, also STED has been applied in the study of chromatin organization at the nanoscale. It has been used in detecting chromatin interaction with the Nuclear Pore Complex (NPC), to study proteins involved in DNA damage response [61] and in DNA replication [62]. In all these studies, STED provided important details thanks to the resolution achieved [63].

Structured Illumination Microscopy

Another interesting super-resolution technique is Structured illumination microscopy. SIM comprises traditional interference-based linear 2D and 3D SIM [64, 65, 66], based on a widefield illumination, and also newly introduced point scanning SIM approaches, which are based on confocal setups [67-70].

SIM, equipped with high NA objectives, can only double the final resolution, achieving almost 100nm in the lateral and 300nm in the axial resolution. The use of low-power laser makes SIM the gentlest super-resolution technique. Indeed, it is well suitable for long time-lapse acquisitions and live-cell imaging, thanks to its low phototoxicity [71].

Single-point laser scanning SIM is a confocal-based technique that considers the focal spot as a structured illumination. In confocal acquisitions the narrowing of the pinhole significantly reduces the acquired fluorescent signal. To overcome this limitation, it is possible to substitute the pinhole with a detector array and ‘reassign’ photons positions on the detector [67]. Muller and Enderlein performed confocal acquisition and detection with a CCD camera, reconstructing the image by reassigning the information acquired from each position of the confocal scan [68]. An improvement of this has been performed

by York and collaborators [69], by collecting the information from hundreds of confocal illumination spots onto a CCD camera, reconstructing the image by using the information from each confocal illumination spots, thus performing a virtual pin-holing the acquisitions.

Classic interference-based SIM, which from now on will be referred to as SR-SIM, is based on a widefield microscopy setup with a mobile diffraction crystal added into the excitation path. Thanks to a mask the zero and ± 1 order diffracted laser beam can pass through the objective to perform 3D acquisition, while, to perform 2D acquisitions, only the +-1 are allowed to pass. At the focal plane of the objective the laser beams interfere with each other creating a striped illumination. The superimposition of the sample and the pattern illumination generates an interference effect, which creates the Moiré fringes.

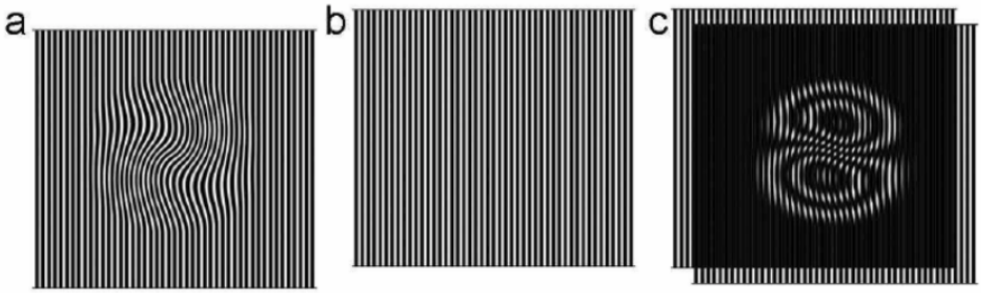

Figure 1.6 The Moiré effect. The superimposition of a fine detail sample, **a)**, and a structure pattern, **b)** give rise to a patterned image, **c)** which contains the information from (a) and (b), but also the information raised by the moiré effect. The original fine detailed image can be extracted by acquiring multiple acquisitions and performing computational processing (image credit: Heyesong Lee, UCLA).

The overlapping of high-frequency features of the sample – which are sub-diffraction information - and the high-frequency of the structured illumination creates a low-frequency pattern which can be collected by the objective. To illuminate all the sample and to acquire all the sub-diffraction features, the crystal grating block is moved to phase-shift the pattern and the mask is rotated to acquire at least three orientation of the pattern illumination. Thus, to reconstruct the final SR image, several raw images need to be acquired. In particular, three-phase images for three orientations (9 images) to perform 2D-SIM, and five-phase images for three orientations (15 images) to perform 3D-SIM.

To understand how SIM works we need to start from a widefield microscope, in which the illumination, $I_{ex}(x)$, is unvarying and the spatial resolution is limited by the PSF, indeed the image, $I_{em}(x)$, will be

$$I_{em}(x) = \left(I_{ex}(x)s(x)\right) \otimes PSF_{em}(\mathrm{x})$$

In which $\otimes$ stands for convolution and PSF_{em} is the image of a point-like source (i.e. the emission point spread function). The resolution achievable with a widefield microscope is limited by the $PSF_{em}(\mathrm{x})$ to $\lambda_{em}/2NA$ considering that NA is the numerical aperture of the objective lens.

The use of a structured illumination allows accessing sub-diffraction feature. Indeed, the Fourier transformation equation will be

$$I_{em}(k) = \left(I_{ex}(k) \otimes S(k)\right)H_{em}(\mathrm{k})$$

With $I_{em}(k)$, $I_{ex}(k)$, $S(k)$ and $H_{em}(k)$ that are the Fourier transforms of $I_{em}(x)$, $I_{ex}(x)$, $S(x)$ and $PSF_{em}(x)$. The $H_{em}(k)$ is the detection passband, or Optical Transfer Function (OTF), which has a cut-off spatial frequency $K_{em} = 2NA/\lambda_{em}$ as shown in figure 1.5.

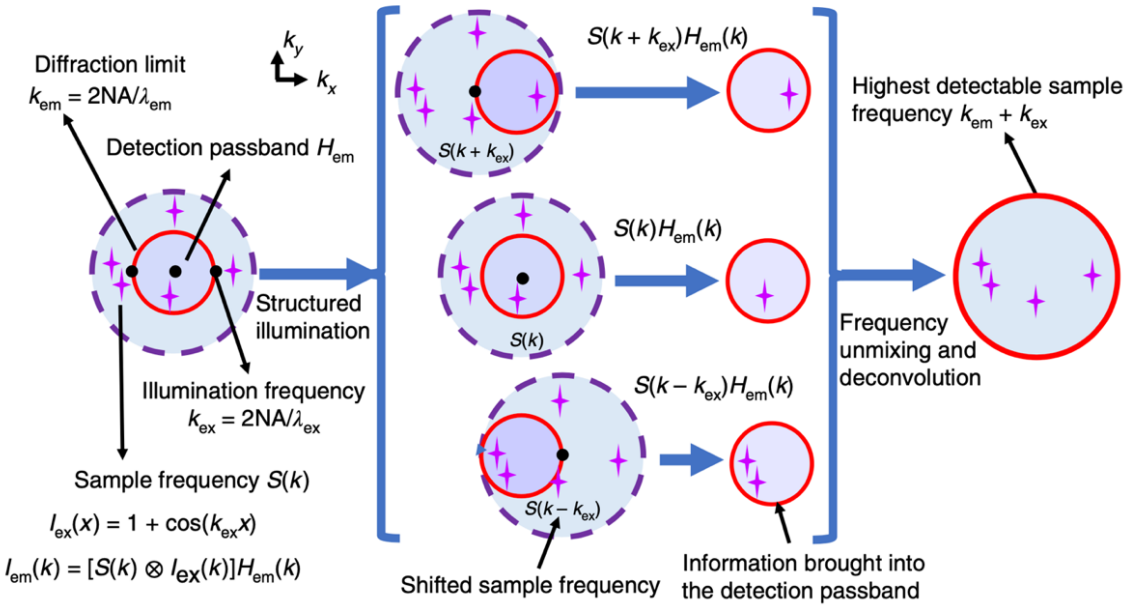

Figure 1.7. Scheme of traditional interference-based SR-SIM frequency domain. In traditional SIM, the interference between two or three laser beams creates a 2D or 3D interference pattern. This pattern has a spatial frequency k_{ex} in the sample focal plane. This illumination pattern shifts the sample's spatial frequency spectrum $S(k)$ to

$S(k + k_{ex})$ and $S(k - k_{ex})$, translating sub-diffraction high-resolution information into the diffraction-limited detection passband $H_{em}(k)$ that has a cutoff spatial frequency k_{em}. Thanks to computational processing, it is possible to extend the maximum detectable frequency to $k_{em} + k_{ex}$. (Image credit. Yicong Wu and Hari Shroff) [65].

In figure 1.7 it is shown how the interference of laser beams creates an interference pattern characterized by k_{ex} illumination frequency. k_{ex} allows shifting the sample spatial frequency spectrum from $S(k)$ to $S(k + k_{ex})$ and $S(k - k_{ex})$, thus moving the SR information within the diffraction passband $H_{em}(\mathrm{k})$. After computational processing, which includes frequency unmixing and deconvolution, it is possible to extend the observable frequencies from k_{em} to $(k_{em} + k_{ex})$ [65].

To summarize, SR-SIM increases both the lateral and axial resolution compared to a widefield microscope. Compared to SMLM which requires ten thousand frames, or STED which is a laser scanning technique, SIM is also very well-suited to perform 4D imaging at a fast frame rate because it only needs 9 or 15 raw acquisitions to perform respectively 2D/3D-SIM. Another advantage of SR-SIM is that it can be performed using conventional antibodies and it does not require photo-switchable fluorophores. This also allows the possibility of performing up to 4 color multichannel acquisitions whereas other SR techniques are often limited to 2 color acquisitions.

On the downside, traditional SR-SIM does not reach ~20nm SMLM or ~50nm STED resolution, thus limiting the use of SR-SIM to studies whose interest is beyond a 100nm resolution. Moreover, in SR-SIM the mathematical post-processing requires a precisely calibrated and aligned setup, correct reconstruction parameters, and correspondence of sample and oil objective refractive index to avoid the formation of reconstruction artifacts that require significant knowledge and counteracts [72]. Another drawback of SR-SIM is that it is highly sensitive to out-of-focus light, meaning that is not the best choice for densely labeled or thick samples. An excellent solution to overcome the background fluorescence limitation in thin samples, < 5um thick, is the combination between 2D-SIM and TIRF microscopy which is characterized by low phototoxicity and great background suppression.

SR-SIM has the potential to be coupled with other SR techniques such as SMLM or STED microscopy. Recently SIM has been coupled with SMLM exploiting the advantages of both techniques and correlating the images acquired with both techniques to minimize imaging artifacts and to improve the final resolution of the reconstructed image [73, 74].

Increasing the resolution beyond a factor of two is possible by exploiting a non-linear or a multilinear response from the sample [75]. Indeed, if the emitted signal of the specimen responds nonlinearly to the illumination pattern, the collected signal will contain information of higher harmonics, due to the non-linear response. Of course, this information will be filtered by the Optical Transfer Function, OTF, of the microscope, but thanks to the structured illumination they will still be mixed to lower frequencies of the pattern, so they will be computationally separatable. In non-linear SIM there are more than three higher-order components, thus, it is necessary to acquire more phases and orientations raw images, to perform an isotropic image reconstruction. On the downside, the acquisition of more images needs a faster acquisition than any cellular process to avoid motion artifacts. The easiest approach to cause a non-linear response of the sample is to illuminate the sample with very high laser intensity inducing a direct singlet state saturation. In the context of widefield illumination, saturation is achievable by using a laser which produces high nanosecond pulses [76]. However, inducing non-linear response brings some disadvantages. The use of a high-power laser to induce a singlet or triplet state can ruin or even destroy the sample due to heat generation. Another disadvantage is that most of the fluorophore will emit fluorescence decreasing the SNR, compared to other SR techniques such as STED, but this problem can be avoided by using photo-switchable or photo-activable dyes [75]. With these ‘tricks’ it is possible to push the resolution down to ~60nm also in time-lapse acquisitions of living cell processes [77].

Since its introduction, SR-SIM proved to be a powerful tool to investigate the nuclear environment within living cells. Schermelleh and collaborators made use of 3D-SIM to analyze chromatin structure and distribution within mammalian cells. They exploited the multicolor capabilities of SIM to simultaneously label the nuclear pore complex, NUP, the nuclear lamina, and

chromatin [78]. After this work, 3D- SIM was used to study the structure of human centrosomes in mitosis and interphase and to study the synaptonemal complex in meiotic chromosomes unrevealing new information about chromatin organization [79, 80]. Also, Markaki and collaborators used 3D-SIM to analyze the nuclear environment, studying the nuclear distribution and topography of DNA replication and transcription in interphase nuclei [81]. Later on, 3D-SIM was involved also in live-cell imaging studies such as in the work of Chagin in which they visualized replication foci down to single replicons [82]. Super-resolution Structured Illumination Microscopy has been used in different scientific fields such as microbiology to study parasite, bacteria, or viral infections, but also in botanical studies to image plant-cell structures [83-90].

Chapter 2

SPLIT-SIM: a novel approach in the reconstruction of SIM microscopy data

Among all the super-resolution techniques available today, mentioned in chapter 1, we choose to work on Structured Illumination Microscopy. Since we were interested in using a 'gentle' super resolution technique, SIM proved to be a good choice in performing multi-color, live-cell imaging studies, but on the downside, it also requires a considerable training and expertise to evaluate the quality of the acquired data.

Most of the developed SIM reconstruction algorithms relies on the spatial frequency domain to access higher frequencies, i.e. sub-diffraction information, thus achieving super-resolution images. Since its introduction, several side-reconstruction algorithms have been proposed [65, 66, 101, 102, 10,104, 105, 106] and, during my Ph.D., I worked on a new and alternative approach: combining the SPLIT algorithm, introduced in Chapter 1, with super-resolution structured illumination microscopy.

In analogy with lifetime-resolved STED, we consider SIM as a multidimensional super-resolution technique. With the term 'multidimensional' we refer to the fact that, in SIM, the final image is obtained by processing multiple images obtained by changing the position of the illumination pattern. We can show that the high-resolution features are encoded in the pattern orientations and translation steps. First, we showed that fluorophores located in different areas of the PSF have different intensity profile fingerprints in relation to the pattern translation steps. Then we demonstrated that we can visualize and analyse this information in the phasor plot, which contains the Fourier Transform of the intensity profile calculated at each pixel of the image.

The different fingerprints of fluorophores are clearly visualized in the phasor plot and their difference can be exploited to calculate the fraction of the total signal corresponding to the center of the PSF, and thus reconstructing a super-resolution final image with higher resolution.

In particular, we believe that the combination of SPLIT with SIM can be a powerful tool for every-day acquisitions and for unskilled users, because the phasor plot allows a direct evaluation of the raw data quality. We will also show that the spatial resolution achievable in the focal plane will be dependent on one parameter and will allow a 2x resolution improvement without performing any deconvolution process.

Considering that SR techniques have became fundamental in the study of chromatin organization in relation to genomic functions, we will also show the application of SPLIT-SIM to the study of chromatin associated proteins, by showing two-color SPLIT-SIM reconstructions of nuclear functional sites.

For the first time, we demonstrate that SPLIT can be applied not only to STED microscopy, but also to another super-resolution technique. Its versatility allowed its application to SIM microscopy, by changing the traditional reconstruction process opening new possibilities.

Main Goal of the project

The main goal of the 'SPLIT-SIM' project is coupling the concept of Separation of photons by lifetime tuning (SPLIT) with Structured Illumination Microscopy (SIM). As introduced in Chapter 1, SPLIT is a recent technique able to perform super resolution by decoding SR images information through an additional channel of the microscope. In Lanzano et al [59] it has been demonstrated the applicability of SPLIT to STED by exploiting, as additional parameter, the different lifetimes between the center (slower lifetime) and the periphery (faster lifetime) of the PSF, induced by the STED laser beam. Instead, in Sarmento et al [60] they explored the versatility of the SPLIT algorithm coupled with STED, by using a different 'additional parameter' which was the different intensities of the STED beam.

The basic idea of the SPLIT principle, schematically is the following: if it is possible to discriminate between a central region and a peripheral one within the observable region of the microscope, then it is possible to separate the

central information from the outer one. In this thesis work we were able to apply the SPLIT algorithm to SIM raw data to perform super-resolution reconstructions of images. To do so, we consider SIM as a multi-dimensional technique whose super-resolution information is ‘hidden’ in the multiple raw images with different phase and angles of the pattern. Therefore, as an ‘additional channel’ we exploited the different illumination of the sample due to the shifting position of the illumination pattern itself. In the end a SPLIT-SIM super-resolution image will be composed by considering only the information coming from the centre of the PSF. In this context we will demonstrate that fluorophores located in the centre of the PSF and fluorophores located in the periphery show different behaviours when we plot the variation of the fluorescence intensity in relation to the illuminating pattern, thus allowing the separation of super-resolution information.

RESULTS

SPLIT-SIM method

To demonstrate the applicability of the SPLIT approach to SIM measurements, we demonstrated that SIM can be considered a multidimensional super-resolution technique in which the super-resolution information are 'hidden' into an additional parameter. In a WF, microscope two fluorophores closer than the diffraction limit will emit simultaneously when excited by the illumination. Therefore, the intensity at any given pixel will be given by a contribution of all fluorophores centered with the pixel position (center of the PSF), but also by fluorophores located within the PSF, as schematized in Fig.2.1a).

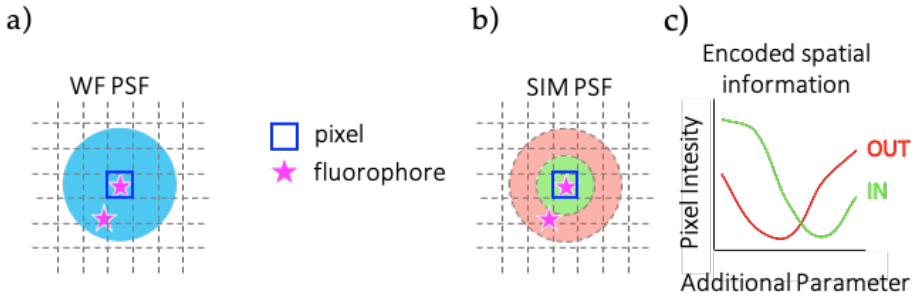

Figure 2.1 SPLIT principle in SIM a) schematic representation of a Widefield diffraction-limited PSF and **b)** schematic representation of a SIM PSF which contains sub-diffraction spatial information that are, **c),** encoded in an additional channel

In structured illumination the sample is not excited homogeneously, instead it is sequentially excited by shifting the phase of the illumination pattern. This shifting pattern encodes sub-diffraction information within the diffraction-limited Point Spread Function of the microscope. In the next figures, 2.2 and 2.3, we will show that fluorophore in the center, 'IN', and fluorophores in the periphery, 'OUT', of the PSF have different fingerprints when the intensity is in relation to the pattern shifted illumination as schematized in Fig. 2.1b).

To demonstrate the applicability of SPLIT to SIM, we started this work by using our microscope data as report to build up MATLAB simulations, as explained in the "materials and methods" section. In figure 2.2 we show a traditional sinusoidal pattern characterized by five phase-shifts and a fluorophore located

in the center of the PSF whose fluorescence depends on the phase-shift of the illuminating pattern. In figure 2.2 the aim is to show the characteristic fingerprint of a 'IN' fluorophore, which is located in the central area of the observation volume.

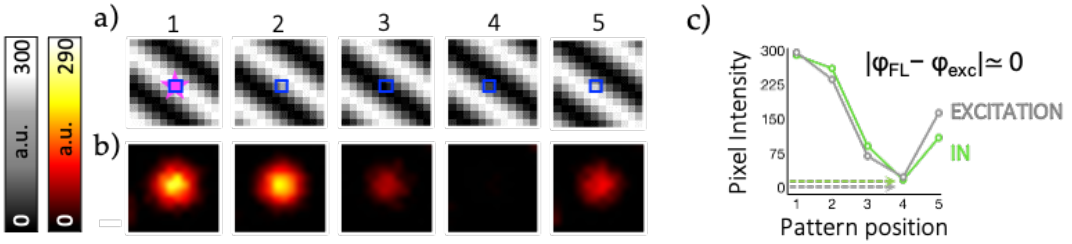

Figure 2.2 Simulation of SPLIT-SIM for a particle aligned with pixel a) Simulation of SIM pattern illumination characterized by 5 phase shifts. **b)** Simulated SIM images of a point-like fluorophore, schematized above as a pink star, centered with the central pixel highlighted as a blue square. Shown are the images of the illumination pattern shifting (1-5) in one direction (greyscale) and the corresponding fluorescence image of the simulated fluorophores (red hot). **c)** Intensity of the central pixel as a function of the position of the pattern. When the fluorophore is centered with the central pixel, the fluorescence intensity (IN) is similar to the intensity of the illumination pattern (EXCITATION).

In figure 2.2 a) it is possible to see that the shift of the pattern illumination, step 1-5, excites differently the fluorescent particle, shown in figure 2.2b). Indeed, due to its phase-shift, the pattern cannot excite homogeneously all the pixels, but it generates a sinusoidal excitation intensity in relation to its phase-shift position. In particular, in each pixel the excitation profile is a sinusoidal wave with phase φ_{exc}. The variation of the fluorescent intensity of a fluorophore, centered with the pixel (representing the region 'IN' of the PSF) is then compared the intensity profiles of the excitation pattern and the fluorescence intensity of the 'IN' fluorophore. In fig. 2.2d) it is shown that the 'IN' fluorophore, has a phase, φ_{FL}, very similar to φ_{exc} , thus

$$|\varphi_{FL} - \varphi_{exc}| \cong 0$$

Subsequently, as shown in figure fig. 2.3, I performed the same analysis on a different pixel. In this case, the fluorophore was not centered with the pixel, i.e it is shifted in the direction of the pattern (representing the periphery region, 'OUT', of the PSF).

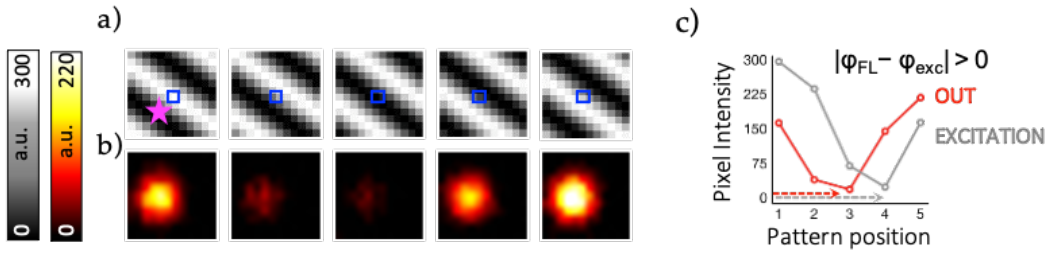

Figure 2.3 Simulation of SPLIT-SIM for a particle non-centered with the pixel a) Simulation of SIM the same pattern illumination shown in figure 2.2a). **b)** Simulated SIM images of a point-like fluorophore schematized as a pink star that is not centered with the central pixel (blue square schematized in fig2.3a). Shown are the images of the illumination pattern shifting in one direction (greyscale) and the corresponding fluorescence image of the simulated fluorophores (red hot). **c)** Intensity of the central pixel as a function of the position of the pattern. When the fluorophore is far from the central pixel, the fluorescence intensity (OUT) has a different behavior compared to the intensity of the illumination pattern (EXCITATION).

In this second case, the fluorescence intensity profile is very different from the one shown previously in fig. 2.2c), indeed in fig. 2.3d) it is shown how the phase of the fluorophore φ_{FL}, is not similar to the pattern phase, φ_{exc} and has a different fingerprint,

$$|\varphi_{FL} - \varphi_{exc}| > 0$$

From the results obtained in figure 2.2 and 2.3, we can state that the profile analysis of the intensity in relation to the pattern position can be used as a fingerprint of the fluorophore localization within the observation volume, the PSF of the microscope.

The algorithm workflow is schematized in figure 2.4 and can be divided in different steps. The first one consists in the microscope acquisition, a SIM stack in which the number of acquisitions depends on the number of phase shift steps, N_{steps}, of the pattern and the number of orientations, N_{angles}. The algorithm considers one orientation at a time, and each orientation comprehends N steps images. In particular, for each orientation, we have a sub-stack $F_{\alpha 1}(x, y, k)$ consisting of N steps slices. The algorithm performs a Fourier Transform, FT, of this sub-stack along the third dimension (see methods) to extract the phasor $P_{FL,\alpha 1}$:

(1)

$$\boldsymbol{P}_{FL,\alpha j}(x,y) = \sum_k F_{\alpha j}(\mathrm{x},\mathrm{y},\mathrm{k})\, e^{i[2\pi h(k-1)/N_{steps}]} \Big/ \sum_k F_{\alpha j}(\mathrm{x},\mathrm{y},\mathrm{k})$$

The phasor $P_{FLj}(x,y)$ has a phase $\phi_{FLj}(x,y)$ and a modulation $M_{FLj}(x,y)$. The pattern profile has a phase $\phi_{exc,1}$ which depends on the illumination pattern parameters and the pixel position.

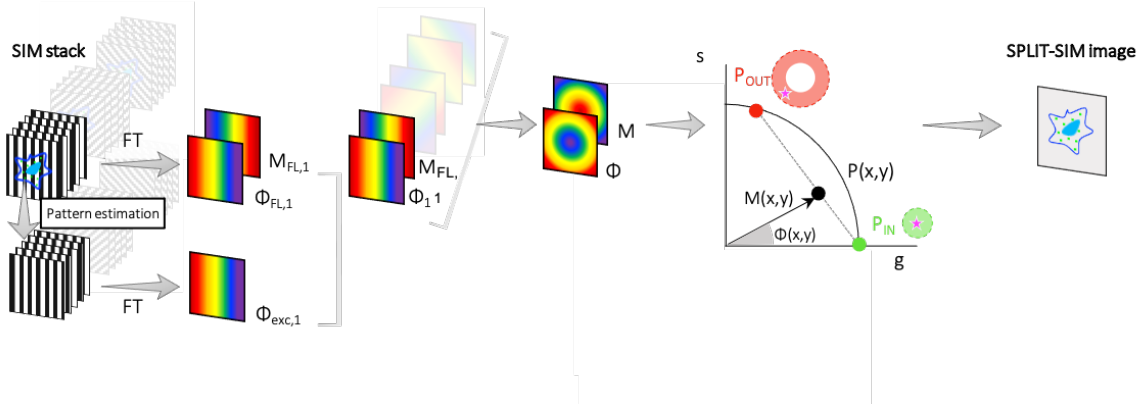

Figure 2.4 SPLIT-SIM workflow scheme. The workflow of SPLIT-SIM starts from the SIM image acquisition stack, on the left, to the formation of the SPLIT−SIM image which consists in the calculation of a modulation and phase image for each orientation of a SIM stack, pattern parameter estimation, correction of the correct phase image for each orientation, calculation of the average phase and modulation images from all the orientation, decomposition in the phasor plot, reconstruction of the super-resolved image.

As shown in fig 2.2d-f) we calculated $\phi_1 = \phi_{FL,1} - \phi_{exc,1}$ and to estimate $\phi_{exc,1}$ the algorithm performs an iterative procedure that we will soon explain. So, for the first orientation we obtain a value of modulation $M_{FL,1}(x,y)$ and a correct value of the phase $\phi_1(x,y)$. Accordingly, the corrected phasor will be

(2)

$$P_{\alpha 1}(x,y) = P_{FL,\alpha 1}(x,y)e^{-i\phi_{exc,1}(x,y)}$$

The same calculation is performed for each sub-stack orientation obtaining $P_{\alpha 1}(x,y), P_{\alpha 2}(x,y), P_{\alpha 3}(x,y)$ and then the average phasor is calculated as

(3)

$$P(x,y) = \frac{\Sigma P_{\alpha j}(x,y)}{N_{angles}}$$

The phasor $P(x,y)$ is then used to generate a super-resolution image by decomposing the phasor into two components. One of these components corresponds to the center of the PSF, P_{IN}, and the other one is related to the periphery of the PSF, P_{OUT}.

In each pixel, the fraction of the total intensity related to the center of the PSF, is calculated as:

(4)

$$f_{in}^{h=1}(x,y) = \frac{[P_{out} - P(x,y)] \cdot (P_{out} - P_{in})}{|P_{out} - P_{in}|^2}$$

The value of f_{in} depends on the distance between the phasor P and the phasor P_{out} along the line that connects the two phasors P_{in} and P_{out}. To better understand this formula, we need to consider the phasors related to single fluorophores whose localization is at different distances from the center of the PSF, f_0. As shown in figure 2.5, if the fluorescent molecule is in the center of the PSF, the phasor will have $\phi = 0$ phase and consequently $f_{in} \sim 1$. Considering a fluorophore located at a distance $T/2$, where T is the period of the pattern illumination, the phasor will have a phase $\phi = \pi$, and $f_{in} \sim 0$. When the fluorophore is located at a distance $d = +d_0$ or at $d = -d_0$ the formula will have the same value because of the choice of $P_{in}(\phi = 0)$ and $P_{in}(\phi = \pi)$ parallel to the x axis.

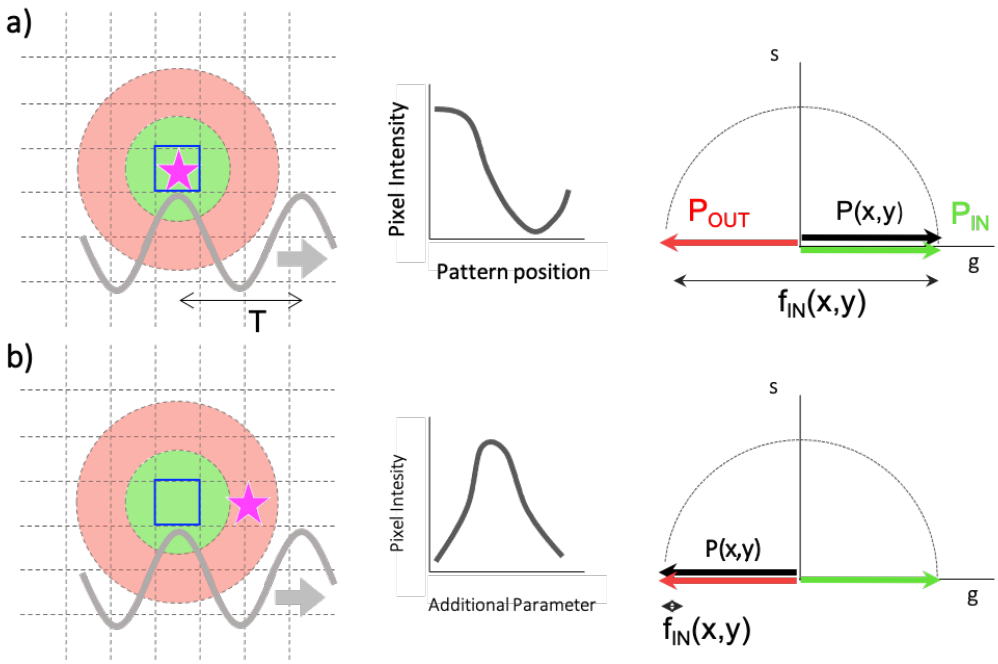

Figure 2.5 Phasors of single fluorophores. a) SPLIT-SIM processing schematic in the case of single fluorophores located in a different position, in relation to the central pixel considered. a-b) the red and green circles schematize SIM PSF and, in grey, it is shown an illumination pattern of period T translating in the direction of the arrow. In the middle there is a line profile intensity of the pixel, blue square, as a function of the pattern position. On the left are shown the decomposition of the corresponding phasor **P**(x,y) of the pixel, in the components $\mathbf{P}_{in}$ and $\mathbf{P}_{out}$. Different positions of the fluorophore (indicated by the pink star) correspond to different phasors and to different values of the calculated fraction $f_{IN}(x,y)$.

Considering a 'real' acquisition, the PSF will contain many fluorophores, thus the resulting phasor will be given by a linear combination of the phasors of each single fluorescent molecule.

Moreover, in the phasor $P^{(h=2)}(x,y)$, the spatial information is contained and related to the second order component of the illumination calculated at harmonic number h=2. This is then used to extract the fraction $f_{in}^{h=2}(x,y)$, as

(5)

$$f_{in}^{h=2}(x,y) = \frac{[P_{out} - P^{(h=2)}(x,y)] \cdot (P_{out} - P_{in})}{|P_{out} - P_{in}|^2}$$

Subsequently, the algorithm combines the information from both harmonics as

(6)

$$f_{in}(x,y) = f^{(h=1)}(x,y) f_{in}^{(h=2)}(x,y).$$

To understand this formula, we have to consider the second order harmonic component, h=2, which gives insights on the spatial information at a finer scale. This because it is characterized by a period of $T_2 = {}^{T}/_{2}$. Consequently, the phasor P_{out} will correspond to a distance from the PSF center ${}^{T_2}/_{2} = {}^{T}/_{4}$. Equation (4) will be used to calculate the information, in terms of fraction of the signal, coming from the center of the PSF. Whilst equation (6) will be used to calculate the fraction of the signal corresponding to the center of the PSF

The final image is then calculated

(7)

$$I_{IN}(x,y) = f_{in}(x,y) I_{WF}(x,y)$$

Where $I_{WF}(x,y)$ correspond to the sum of the intensity of all the slices collected by the SIM microscope.

To summarize, the super-resolution information hidden in the SIM raw data is encoded in the phasor $P(x,y)$ and is used to reconstruct a final image with an improvement in the spatial resolution. A fundamental step in this reconstruction process is the correct estimation of the pattern parameters. This is characterized by its three angles orientation, α_k, by three offset values of the initial position of the pattern, p_k, and by a period, *T*. As shown in figure 2.6, the use or misuse of pattern parameters can be verified by looking at the phase image $\phi(x,y)$. We found that with the correct estimation of the pattern parameters the phase of the image, ϕ_{AV}, is minimized.

Accordingly, the minimization of the value ϕ_{AV} of the image, can be used to evaluate the correct estimation of pattern parameters of any unknown illumination pattern.

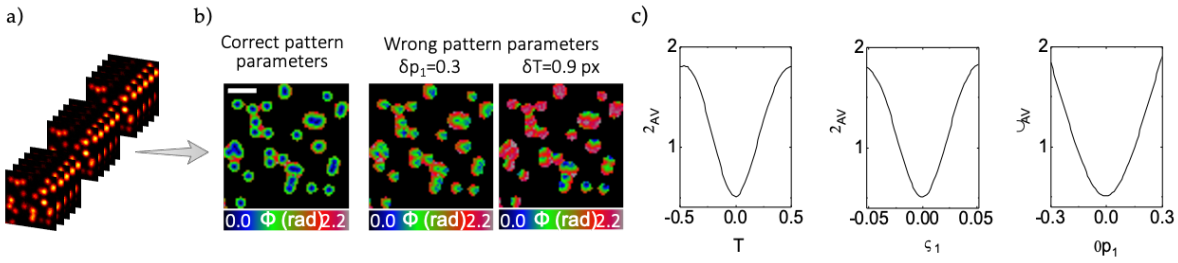

Figure 2.6 Phase estimation in SPLIT-SIM. a) a) Simulated SIM stack acquisition and **b)** relative phase images calculated first with the correct pattern parameters, then with a wrong value of the offset of the first angle (δp_1=0.3) and then with a wrong value of the period (δT=0.9 px). Scale bar 1 μm. **c)** Representations of the average phase value (ϕ_{AV}) in relation to the period (T), the first orientation angle (α_1), and the offset of the first angle (p_1).

SPLIT-SIM Algorithm on 2D-SIM simulated data

Upon the demonstration that SPLIT-SIM can discriminate between 'IN' and 'OUT' fluorophores, we performed SPLIT-SIM reconstructions of 2D-SIM simulation data. The SIM image stack was created by simulating a sinusoidal pattern stack characterized by 3 orientations and five translation steps.

To evaluate our algorithms abilities, we generated image of sparse particles with different conditions of contrast ($C_p = 1$ and $C_p = 0{,}33$) and photon counts, as show in the figure 2.7.

In the first simulation we generated a maximum contrast of pattern illumination with *Cp=1* (figure 2.7a) from which we simulate two different imaging conditions. In the first case, represented in figure 2.7d), we simulate an image with a very high level of photon counts, S, set as S=500, and, in figure 2.7e) we simulated an image with less photon counts, S=5.

The phasor is a 2D histogram representation of the values g and s of all the pixels of the image ($g = Mcos\phi$; $s = Msin\phi$). To simplify the visualization,

the phasor with negative phase values, $-\pi < \varphi' < o$ are always in the first quadrant by setting $\varphi = |\varphi'|$. The resulting phasor from figure 2.7d) shows that high photon counts and maximum pattern contrast leads to a characteristic 'arch' shape.

In the second case, fig. 2.7e), we simulated particles with maximum phase contrast, but low photon count. In this case, the arch is not thin and precise, and is characterized by a spread of points due to the Poisson noise that brings uncertainties to the values of modulation and phase, M and ϕ. This Poisson noise effect can be noted also in the phase and modulation images.

In general, the points with $\phi \cong 0$ are the ones related to the 'IN' fluorophores, the center of the PSF, whilst the points with $\phi > 0$ correspond to the periphery of the observation volume. From the phasor plot it is also possible to see that the value of Modulation is almost constant in all the PSF and its value is approximately $M_{max} = 0{,}5$. As shown in figure 2.7d), the M_{max} value strictly depends on the contrast of the illumination pattern, indeed, if we set $C_p = 0{,}33$, as in figure 2.7f), the M_{max} value drops to $M_{max} = 0{,}16$. Accordingly, we can state that, in the case of sparse particle images, the radius of the arch in the phasor plot is an indicator of the contrast of the illumination pattern. Simulations were also performed on the same intensity signal S samples, with a lower contrast pattern, as shown in figure 2.7 f-g).

Additionally, crowded sample simulations were performed. In this case the illumination contrast was the maximum, figure 2.7a), and the photon count was S=500, as shown in figure 2.7d). In figure 2.7h) we can see that the value of modulation is lower than the value M_{max} found in the first sample (figure 2.7d) and that in the phasor plot we cannot see the charismatic arch shape.

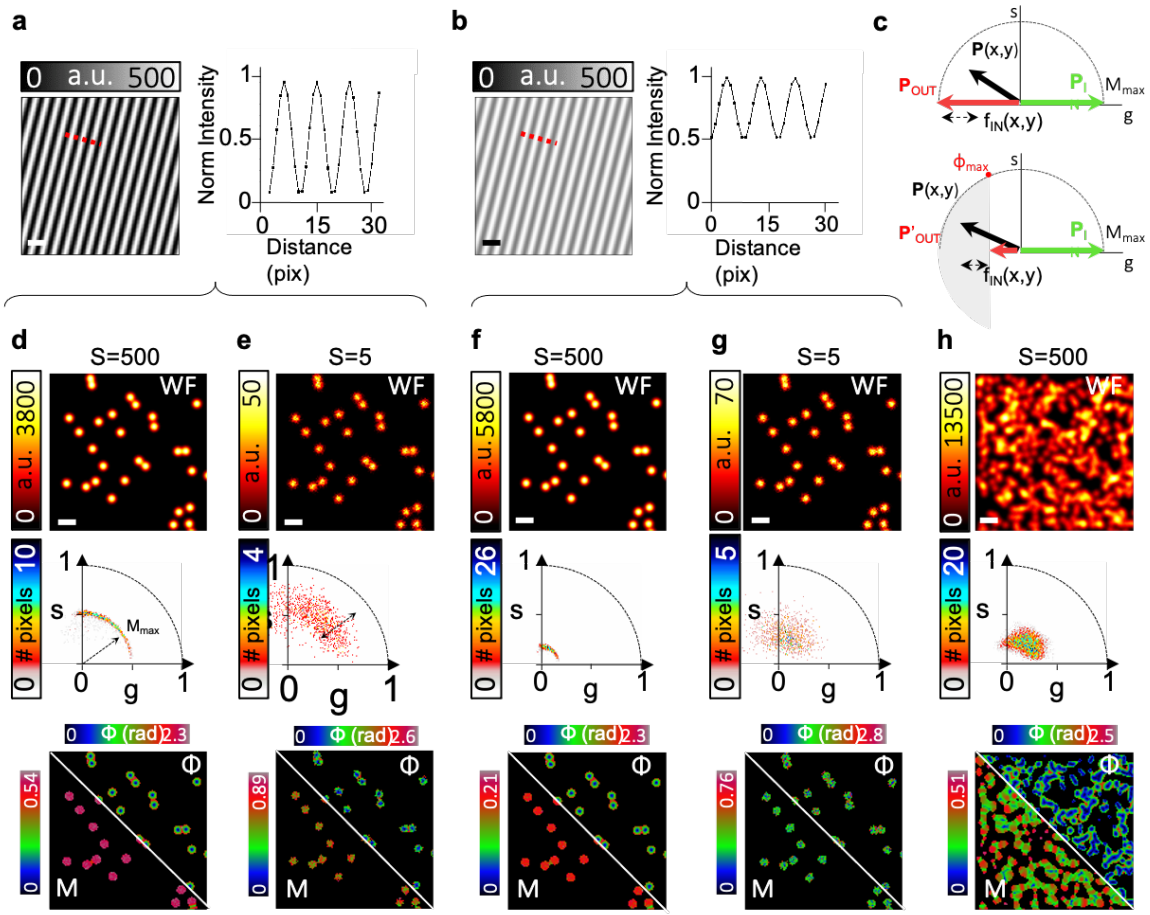

Figure 2.7 SPLIT-SIM applied to Simulated SIM images of point-like sources. **a)** Simulation of a periodic illumination pattern characterized by maximum contrast (C_p=1) and its corresponding line intensity profile along the red dashed line. **b)** Simulation of a periodic illumination pattern with lower contrast (C_p=0.33) and the corresponding line intensity profile along the red dashed line. **c)** Schematic showing the possible setting of the phasors P_{in} and P_{out}. **(d-g)** SPLIT−SIM of simulated SIM images of sparse point-like sources with maximum (d-e) and minimum (f-g) pattern contrast and different noise level, as defined by the intensity level S. From top to bottom, we show the widefield image, obtained by summing all the slices of the stack (WF), the phasor plot, the modulation (M) and phase (ϕ) image. **h)** Same as in (d), but simulating a crowded object. Scale bar 700 nm.

With these simulations we are able to extract the P_{in} and the P_{out} values, which respectively correspond to the center and the periphery of the PSF. To reconstruct the final super-resolution image we need to set the position of the phasor related to the center of the PSF, $P_{in} = M_{max}\exp(i\phi_{in})$ characterized by $\phi_{in} = 0$, and the position related to the phasor corresponding to the periphery of the PSF, where $P_{out} = M_{max}\exp(i\phi_{out})$ and $\phi_{out} = \pi$. Considering that all the phasors yield M<M_{max} this sets the value of the fraction f_{IN} to be only between 0< f_{IN}< 1. Yet, if we set $P'_{out} =$

$M' \exp(i\phi_{out})$, with $\phi_{out} = \pi$, and $M' = M_{max}\cos(-\phi_{\max})$, with $\phi_{\max}$ that is a tunable parameter, equation 4 can now have negative values as shown in the bottom of figure 2.7c. In this case the values of the fraction are made to fall between 0 and 1 by utilizing a non-linear filter, as explained in the method section. This particular choice achieves an improvement of the spatial resolution, but can introduce artifacts in the final image. For this reason, we investigated the effect of using different $\phi_{\max}$ values on a simulated Siemens star pattern, shown in figure 2.8. Here we see that the artifacts arise when we set values of $\phi_{\max} < 0.5\pi$. Accordingly, we set $\phi_{\max} = 0.5\pi$ as the lower limit to be used.

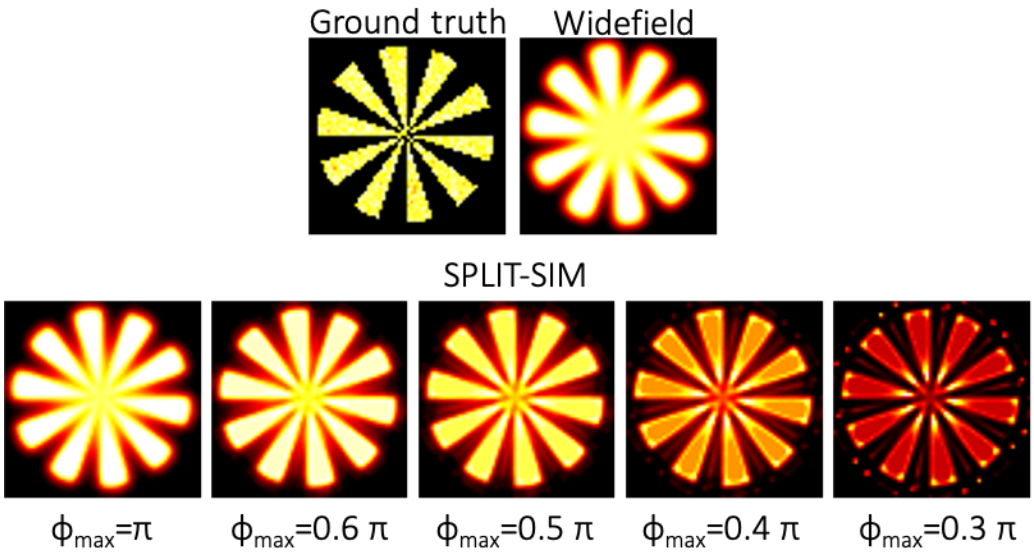

Figure 2.8 Siemens star pattern simulations to evaluate the onset of artifacts. The top row shows the siemens star object used for the simulation, Ground truth, and its widefield image. The bottom row shows SPLIT-SIM reconstructions performed with different ϕ_{max} values.

In summary, we can say that the phasor plot is a valuable and useful tool to intuitively understand different information from SIM raw data. Namely, we can directly evaluate the pattern contrast by only looking at the radius of the "arch" shape of the phasor. Moreover, we can computationally evaluate the maximum resolution achievable with experimental levels of photon counts through the spreading of points in the radial and angular coordinates. As a consequence, as seen in figure 2.7d-g), the worst SPLIT-SIM reconstructions are the ones performed on the sample with low photon counts and low pattern contrast. However, this intuitive representation of

the arched phasor plot is available only in the case of imaging sparse molecules, whilst in the case of crowded sample this is not clearly visible.

SPLIT-SIM performs 3D super-resolution reconstructions without deconvolution

After testing the algorithm on simulated samples, we tested our algorithm with experimental data. We performed 3D-SIM acquisitions of fluorescent microspheres with a N-SIM microscope. For this test our samples was prepared by diluting the beads stock solution onto a coverglass in order to have sparse beads, to recognize in the phasor plot the typical 'arch-shape'. We performed the analysis on a sample in focus at plane z=0 nm, and in figure 2.10 we show both the phasor plot related to the first and the second harmonic frequencies of the FT, as shown in the methods.

The values of the M_{max} in the two different harmonics *are* $M_{max\ h1}$=0.39 for the first one and $M_{max\ h2}$=*0.27* for the second value. This difference in the values of the two M_{max}, relies on the fact that in the first and second order of the pattern we have different contrasts.

The arch related to the second harmonic, figure 2.10c), shows a wider angle, which is in agreement with the spatial information contained at higher frequencies, and is also visible in the relative phase image. We use the information from both harmonics in the SPLIT-SIM algorithm to obtain the image, figure 2.10d), by setting $\phi_{\max} = 0.5\pi$. To evaluate the resolution of the reconstructed image we use Image Correlation Spectroscopy, ICS [107]. The resolution calculated by the auto correlation function (ACF) of the Widefield image was $FWHM_{WF}$= 282 nm, while the resolution of the SPLIT image was $FWHM_{SPLIT}$=130 nm, corresponding to a two-fold improvement. Therefore, we compared our reconstruction with the one made by the manufacturer's software, which is Nikon NIS elements. The NIS software uses deconvolution and the ACF revealed a resolution of $FWHM_{NIS}$=156 nm. In this comparison we want to underline that our results are obtained without performing any deconvolution process. However, our results is also obtained by pushing our tunable parameter $\phi_{\max}$, towards its limit, $\phi_{\max} = 0.5\pi$, while if we set a lower value of $\phi_{\max}$, such as $\phi_{\max} = \pi$, the ACF calculates a

$FWHM_{SPLIT}$=210 nm, which corresponds to more or less 1.3 fold improvement in resolution.

In SIM it is possible to perform optical sectioning, indeed the interference between three laser beams creates not only a patterned illumination in x,y, but also in the z-axis, as shown in figure 2.9.

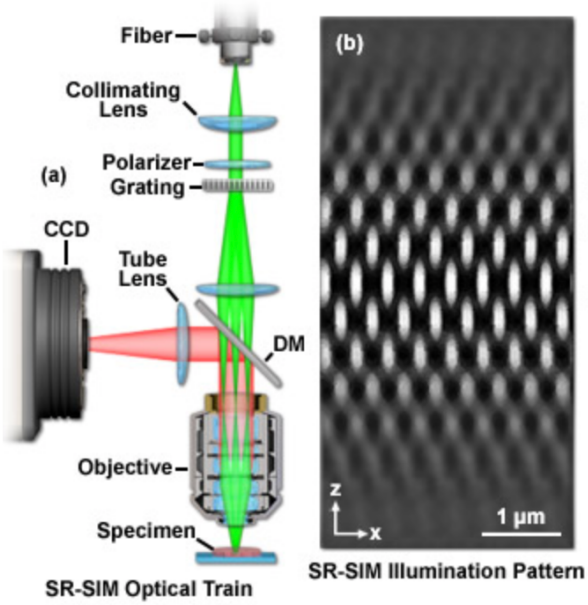

Figure 2.9 SIM 3D pattern. **a)** schematic of SIM illumination path. the laser beam passes through a polarizer and the diffraction grating. Only the 0, -1, and +1 diffraction orders are focused onto the objective rear aperture then collimated in the specimen focal plane where they interfere generating a 3D (lateral and axial) sinusoidal illumination pattern shown in **(b).** (image credit. Zeiss.edu)

To obtain three-dimensional information, a z-stack acquisition is performed. We analyze the microspheres sample on focus, z=0nm, shown in figure 2.10a-e), and then we analyze the same beads at a different focal plane z=300nm, figure 2.10f). In this particular case the beads are out of focus, thus they can be considered at the periphery of the PSF in the z axis. We can see in figure 2.10g), that in the case of an out-of-focus plane the signal yields a lower modulation and the phase and has a shift of $\sim\pi$. Thus, the algorithm then removes from the reconstructed final image the out-of-focus signal by assigning it to the 'OUT' image and consequently, the algorithm assign very few photons to the 'IN' component. This shows us that SPLIT can efficiently evaluate the localization of molecule in the periphery of the PSF also in the z-axis, thus performing an appropriate optical sectioning both in the simulations with $\phi_{\max} = \pi$ and in the simluation with $\phi_{\max} = 0.5\pi$, figure 2.10j).

To summarize, in our algorithm the improvement in resolution is strictly related to the parameter $\phi_{\max}$. In particular, the smaller $\phi_{\max}$ is the more the

final image will be resolved. Setting $\phi_{\max} = \pi$ allows optical sectioning to be performed, but only yields a small improvement in the resolution. Otherwise, by setting $\phi_{\max} = 0{,}5\,\pi$ a two-fold resolution improvement and optical sectioning is achieved.

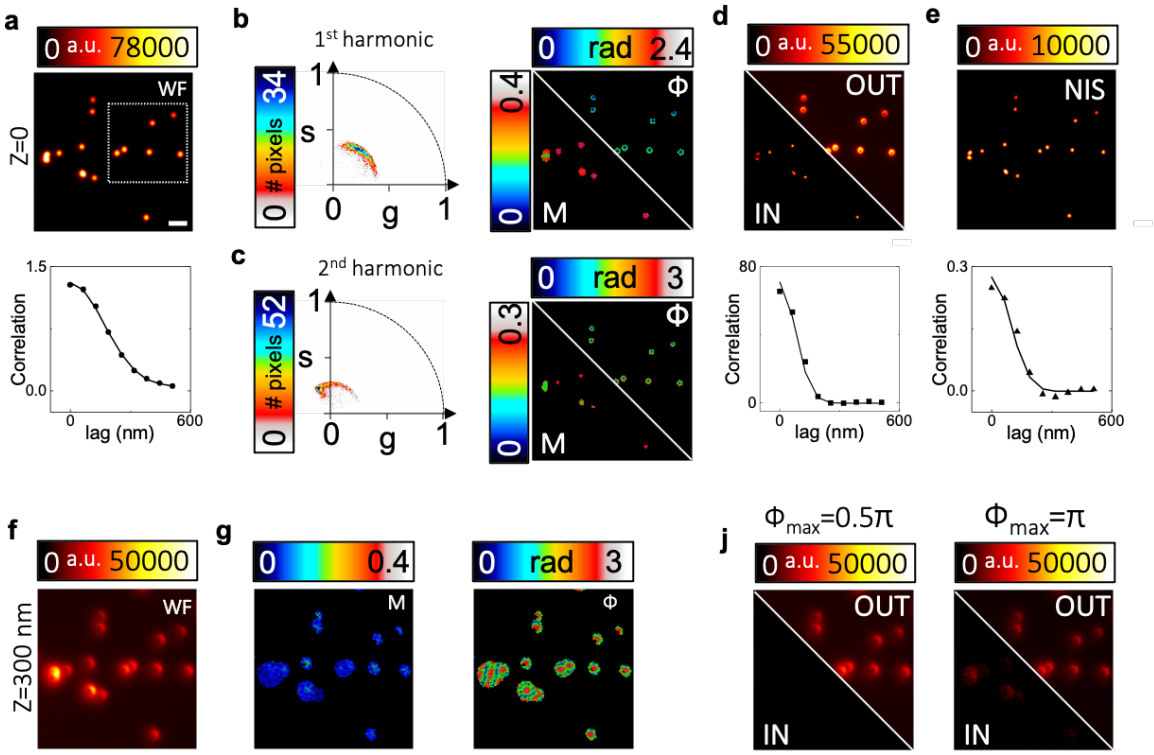

Figure 2.10 SPLIT-SIM on Yellow-Green fluorescent spheres. a) Widefield acquisition of 100-nm YG fluo-spheres and their Auto Correlation Function (ACF) calculated within the dashed box. **b)** 1st harmonic Phasor plot and on the right the relative phase and modulation images. **c)** Phasor plot of the 2nd harmonic and on the right corresponding phase and modulation images. **d)** SPLIT-SIM image, IN, calculated with ϕ_{max}=0.5π, image of the residual component related to the periphery of the PSF (OUT) and ACF of the SPLIT-SIM image in the box below. **e)** NIS Elements reconstruction and corresponding ACF. Scale bar 1μm. **f)** beads shown in a) but in an out of focus plane, 300nm above the focal plane in the z direction. j) reconstructed out-ot-focus images with $\phi_{\max} = 0.5\pi$ and $\phi_{\max} = \pi$ respectively.

SPLIT-SIM applied to the investigation of biological samples

The main goal of our work was applying our algorithm in the reconstruction of biological sample acquisitions. Here we will show 3D-SIM acquisition of Hela cells in which we labeled the histones H2B. We performed SPLIT reconstruction by setting $\phi_{\max} = 0.5\pi$ and $\phi_{\max} = \pi$, respectively in figure 2.11c) and 2.11d), and then we analyse them in comparison with the

Widefield (WF) image, Fig. 2.11a), and with the Nikon NIS elements reconstruction, fig. 2.11b).

With the use of ICS, we analyzed the images and found that the structures formed by H2B staining have an apparent size of $FWHM_{WF}$= *337 nm*, in the WF image, $FWHM_{NIS}$=*156 nm* in the NIS elements reconstruction, and $FWHM_{SPLIT(0,5\pi)}$ = *158 nm*, in the SPLIT image. Setting $\phi_{\max} = \pi$ forms a confocal-like image, with $FWHM_{SPLIT(\pi)}$ = *219 nm* resolution, because the algorithm performs mainly optical sectioning, as shown in fig. 2.11d).

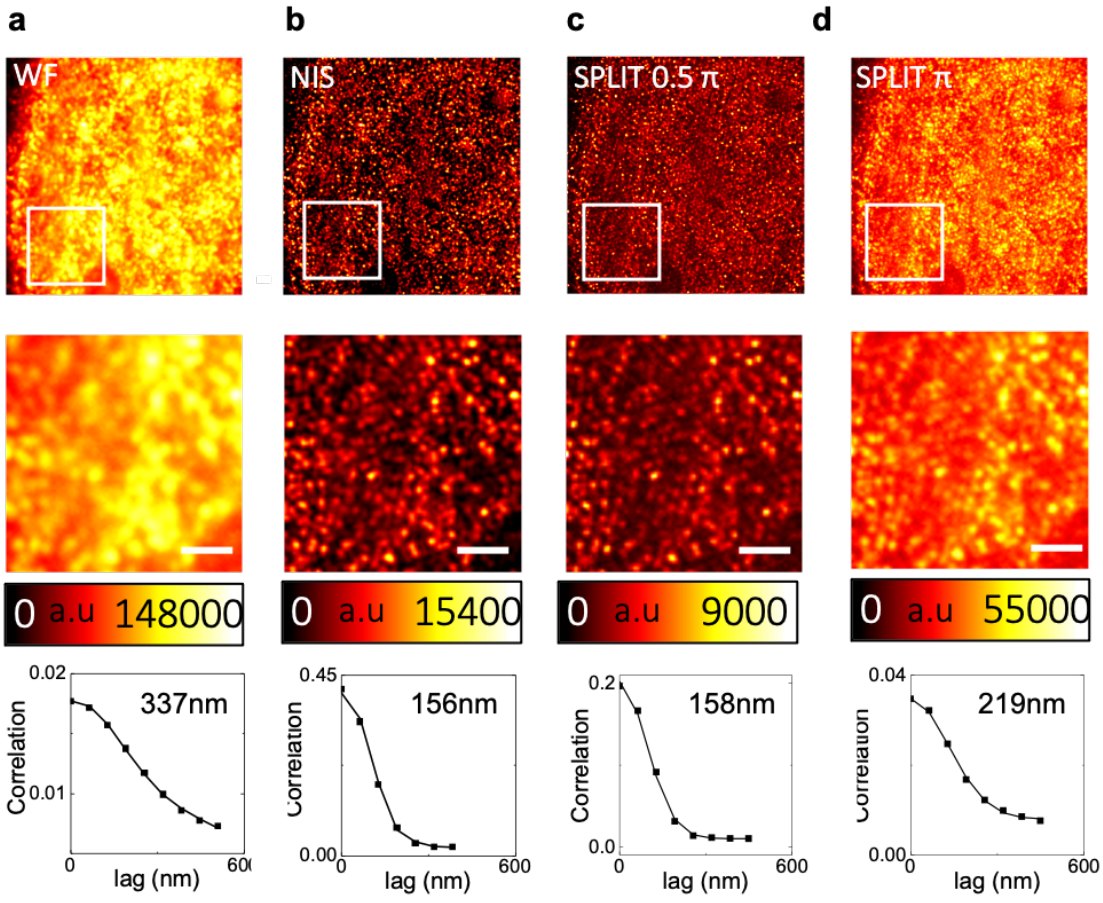

Figure 2.11 SPLIT-SIM imaging of the histone H2B. Top row shows 256x256 ROI, middle row shows 80x80 ROI and bottom row shows the resolution calculated by ACF in the 80x80 ROI **a)** Widefield acquisition **b)** Nikon NIS elements reconstruction **c)** SPLIT-SIM reconstruction with ϕ_{max}=0.5π. **d)** SPLIT-SIM reconstruction with ϕ_{max}=π. Scalebar 1 μm.

Then we used SPLIT-SIM to perform two color image reconstruction of nuclear sites in MCF7 cells. We labeled two different samples: in the first one we stained replication foci by incorporating a nucleotide analogue, EdU, that labels nascent DNA, and a protein involved in the process of replication of DNA, the proliferating cell nuclear antigen, PCNA [110]. In the second specimen, we labeled RNA Polymerase 2 (RNApol2), as a marker of active transcription, and the transcriptionally repressive histone marker (H3K9me3). In particular, in figure 2.12, we show the different resolution achieved in both samples by using $\phi_{max}=0.5\pi$ or $\phi_{max}=\pi$.

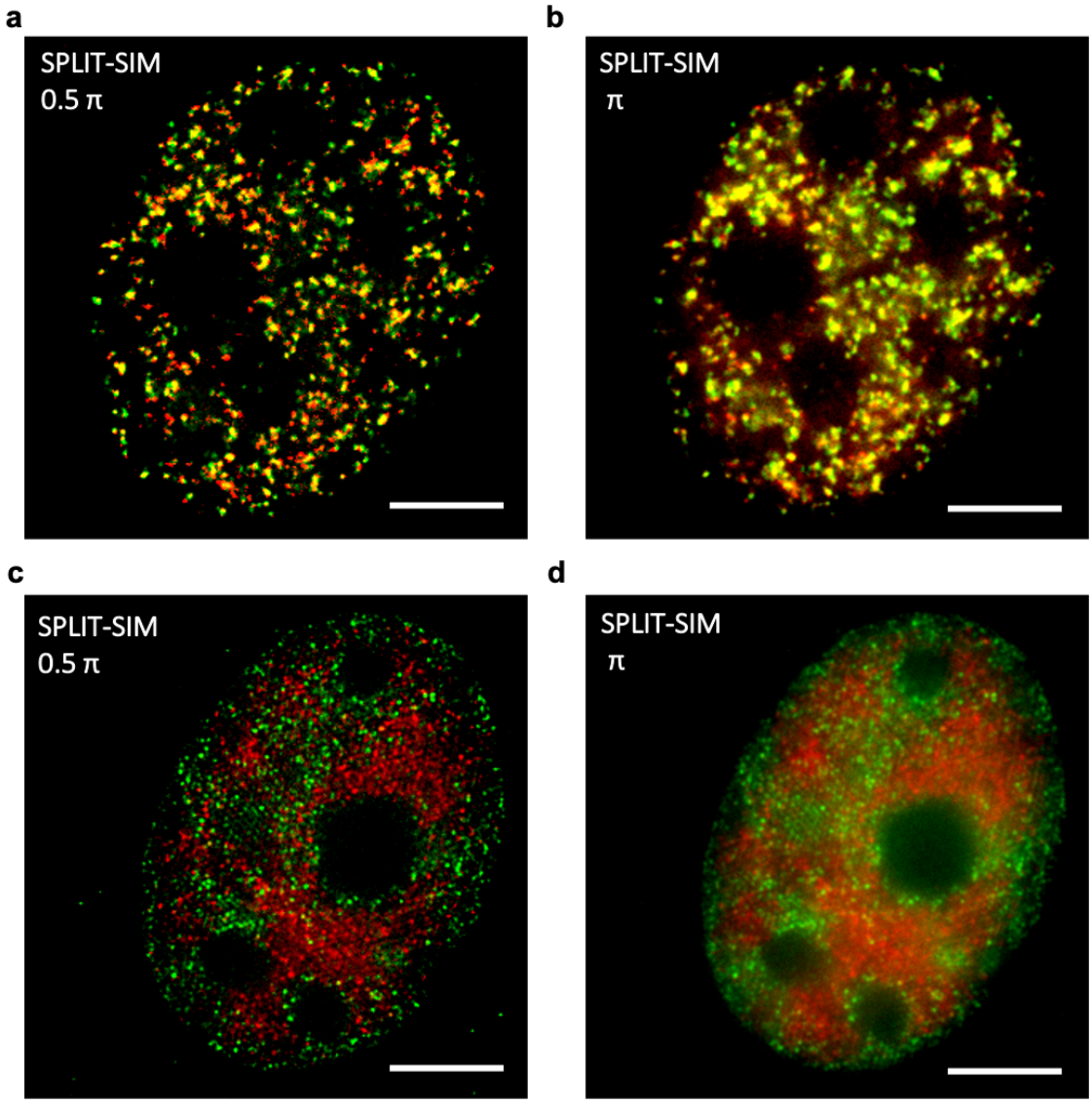

Figure 2.12 Two-color SPLIT-SIM reconstruction of nuclear foci. a-b) SPLIT-SIM reconstruction of PCNA, in red, and EdU in green with $\phi_{max}=0.5\pi$ (a) and $\phi_{max}=\pi$ (b). **c-d)** SPLIT-SIM reconstruction of RNApol2ser2, in red, and histone H3K9me2 in green with $\phi_{max}=0.5\pi$ (c) and $\phi_{max}=\pi$ (d). Scale bar 5μm.

MATERIALS AND METHODS

Simulations

A sinusoidal SIM-like pattern was simulated in Matlab as:

(8)

$$I_{\alpha_i}(x, y, k) = 1 - m\, sin^2\left[h\pi\left(\frac{xcos\alpha_i - ysin\alpha_i}{T} + \frac{k}{5} + p_{i,h}\right)\right]$$

Where α_i is the angle of the pattern, *m* is a constant from 0 to 1, *T* is the period of the pattern, $p_{i,h}$ is the offset of the pattern at the orientation α_i, and *h* is a constant representing the order of the pattern set to 1. The angles of the patter were set as α_1=2.895 rad, $\alpha_2 = \alpha_1 + \pi/3$, $\alpha_3 = \alpha_1 + 2\pi/3$ and the contrast of the pattern, C_P, is defined as the amplitude of the pattern divided by the average and is given by $C_P = (m/2)/(1 - m/2)$. The period, *T*, was set as *T*=630nm, unless specified otherwise, and the position of the pattern was shifted by changing the value *k* from 1 to 5.

With this pattern illumination, simulation of SIM Point-like sources images was performed using Matlab, and consisted of using a variable number of simulated molecules randomly spread in a 128x128 pixel image whose pixel size was set to be 70nm. For each image of the simulated SIM stack, the object image was multiplicated for the simulated pattern $I_{\alpha_i}(x, y, k)$ and then convolved with a Gaussian PSF whose waist size was set as $w_{WF} = 4.5\, pixels = 315nm$. Then, the maximum value of the collectable number of photons, from the object image, in each frame of the stack was set as *S*. Additionally the presence of noise was simulated using the Matlab function 'imnoise' to add to each image a Poisson noise, dependent on the number of counts of each pixel.

SPLIT-SIM Algorithm

The SPLIT-SIM algorithm was implemented in Matlab. The algorithm operates on SIM image stacks $F_{\alpha i}(x,y,k)$ characterized by N_{angles} orientations and N_{steps} pattern translation steps for each angle. For each orientation α_j, the complex number $P_{FL,\,\alpha i}(x,y)$ is calculated through a Fourier Transform according to Eq.1. The phase and modulation, $\phi_{FL,j}(x,y)$ and $M_{FL,j}(x,y)$ are calculated as the modulus of $P_{FL,\,\alpha i}(x,y)$.

A periodic pattern $I_{\alpha j}(x,y,k)$ is simulated, both in the first and in the second harmonic, in concordance with Equation 8 by setting the period as $T=T_{est}$, the orientation angle to $\alpha_j=\alpha_{j,est}$, and the pattern offset to $p_{j,h}=p_{j,h,est}$. These values, i.e. T_{est}, $\alpha_{j,est}$, $p_{j,h,est}$, depict the best estimation of the parameters to describe the experimental illumination pattern. The phasor of the excitation intensity $\mathbf{P}_{exc,j}(x,y)$ is calculated as:

(9)

$$P_{exc,\alpha j}(x,y) = \sum_k I(x,y,k)\, e^{i\left[2\pi h(k-1)/N_{steps}\right]} \Big/ \sum_k I_{\alpha j}(x,y,k)$$

The phase of the pattern $\phi_{exc,j}(x,y)$ is then calculated as the phase of $P_{exc,j}(x,y)$. The corrected phasor $P_{\alpha j}(x,y)$ is calculated according to Eq.9 and this procedure is repeated for j=1….N_{angles}. Then the average phasor P(x,y) that corresponds to the average of the N_{angles}, is calculated by using equation 3.

The phase image ϕ(x,y), calculated as the phase of **P**(x,y), is then used to estimate the illumination pattern parameters. While the values T_{est} (pattern period), $\alpha_{j,est}$ (orientation angles), $p_{j,1,est}$ (first order offsets) are first estimated as the values that minimize the average value of the first-harmonic phase in an image, $\phi_{AV} = <\phi(x,y)>$, where the brackets denote averaging over all the non-background pixels.

Next, the offset of the second order, $p_{j,2,est}$, can be expressed as $p_{j,2,est}= p_{j,1,est} + \Delta p_{j,2,est}$, where $\Delta p_{j,2,est}$ is dependent on the shape of the pattern. The values $\Delta p_{j,2,est}$ are estimated as the value that minimizes the average value of the second order phase in an image, $\phi^{(h=2)}_{AV}=<\phi^{(h=2)}(x,y)>$. To speed-up processing during reconstruction the values of T_{est}, $\alpha_{j,est}$ and $\Delta p_{j,2,est}$ are

calibrated (using a sample of 100-nm fluorescent spheres) and stored into a file. In this way, for any given sample, we must estimate only the parameter $p_{j,1,est}$.

The phasor plots are 2D histogram of the values g and s, respectively $g(x,y) = M(x,y)\cos|\phi(x,y)|$ and $s(x,y) = M(x,y)\sin|\phi(x,y)|$, which corresponds to the modulation and phase images $M(x,y)$ and $\phi(x,y)$.
In each pixel, the fraction of photons corresponding to the center of the PSF $f_{IN}(x,y)$ was calculated using Eq.4-6 (experimental data) or only Eq.4 (simulations). In the experimental data, the parameter M_{max}, that depends on the contrast of the experimental pattern, was determined by imaging a model sample, the sparse 100-nm fluorescent spheres. The parameter ϕ_{max} was set as specified. To force the values of the fraction to fall between 0 and 1, the values of $f_{IN}(x,y)$ were filtered through a logistic function: $f = 1/(1+\exp\left(-k_L\left(f^{-\frac{1}{2}}\right)\right))$ with $k_L = 4$. The remaining fraction of photons, related to the periphery of the PSF, are calculated as
$f_{OUT}(x,y) = 1 - f_{IN}(x,y)$.
To conclude, the super-resolution SPLIT-SIM image was calculated as:

$$I_{SPLIT}(x,y) = f_{in}(x,y)I_{WF}(x,y) \quad (10)$$

Where $I_{WF}(x,y)$ correspond to the sum of all the slices of the stack, $I_{WF}(x,y) = \Sigma_{j,k}F_{\alpha}(x,y)$. Then, the residual image was calculated as

$$I_{OUT}(x,y) = f_{out}(x,y)I_{WF}(x,y) \quad (11)$$

Samples

The first sample involved in our work were 100-nm Yellow-Green beads, Yellow-green FluoSpheres Carboxylate-Modified Microspheres, F8803, Invitrogen. The cover glasses were treated for 20 minutes at room temperature, with Sigma Poly-L-lysine (Sigma Aldrich, P8920). Then we diluted the microspheres in Milli-Q water and we incubated them for 10 minutes onto the coverglass [1:10000 v/v]. Next, the sample was washed twice with

Milli-Q water, dried underneath nitrogen flow and mounted overnight with ProLong Diamond Antifade Mounting Medium (P36965).
Then we moved to biological samples and we used Hela cells and MCF7.
HeLa and MCF7 cells were grown in Dulbecco's modified Eagle's medium (DMEM) (Sigma Aldrich) integrated with 10% Fetal Bovine Serum (Euroclone ECS0180L) and 1% penicillin/streptomycin (Sigma Aldrich). For each line, cells were grown in their flasks and then transferred to 14mm glass coverslips.

Immunostaining

The fixation of Hela cells to stain histone H2B, was different in respect to the other samples and it was performed for 10 minutes with 100% ethanol at -20°, then they were washed two times for 5 minutes in 3% BSA. Then they were incubated in Sigma-Aldrich Normal Goat Serum (NS02L) with 0.2% Sigma-Aldrich Triton 100X in PBS for 1hour at Room Temperature, RT. The immunostaining of histone H2B was performed by using a dilution [1:500] of Abcam rabbit Anti-histone H2B antibody- ChIP Grade, (ab1790) in 5% Normal Goat Serum for 2hours. Upon incubation the sample was washed once for 15 minutes in 5% Normal Goat Serum and 0.2% Triton, then twice for 15 minutes in 0.6% Normal Goat Serum and 0.05% Triton 100X in PBS. As secondary antibodies, we used Goat Anti-Mouse IgG H&L (Chromeo 488) (ab60314) in a [1:200] dilution and we incubated the cells in 5% Normal Goat Serum for 1 hour at RT. Finally, the sample was washed once in 5% Normal Goat Serum with 0.2% Triton for 15 minutes and twice in 0.6% Normal Goat Serum with 0.05% Triton 100X for 15 minutes each wash.

The immunostaining of all the other samples was performed after 4% paraformaldehyde (w/v), PFA, fixation at RT for 10 minutes. The Proliferating Cell Nuclear Antigen, PCNA, the RNA polymerases, RNApol2ser2, and the Histone H3K9me2 were performed after 1hour Blocking Buffer (BB) solution incubation at RT. The BB solution consists of 3% Sigma Aldrich Bovine Serum Albumin (BSA) and 0,5% Triton 100X.

The *PCNA* staining was performed overnight at 4°Celsius, by using a dilution [1:2000] of primary antibody Rat anti-PCNA by Chromotek (16D10) in the BB solution. The next morning the sample is washed once in BB solution and twice in the Washing Buffer solution (WB) which is made by 0,2% BSA and 0,06% Triton 100X. Then the cells were incubated with the secondary antibody, which was anti-rat ATTO 594 [1:500] dilution in BB, before being washed once in BB, twice in WB and three times in Phosphate Buffered Saline, PBS, solution.

The RNA polymerases, *RNApol2ser2* that is a marker of elongating DNA, was stained with an 4° Celsius overnight incubation with an Abcam rabbit anti-RNApol2ser2 (ab5095), [1:500] dilution. Then cells were washed once in BB solution and twice in WB. Next, cells were incubated 1-hour at RT with the secondary antibody anti-rabbit ATTO 594 in BB (1/500 dilution). The last washing step was performed as previously described for the PCNA staining.

The last immunostaining concerning the histone *H3K9me2*, was performed after 1h BB incubation, by incubating the primary antibody, Abcam mouse anti-H3K9me2 (ab1220), overnight at 4° Celsius. Next, the sample was washed once in BB and twice in WB, to prepare the 1-hour incubation of the secondary antibody, anti-mouse Alexa 488, [1:1000] dilution. Then it was washed once in BB, twice in WB and thrice in PBS.

The 5-ethynyl-2'-deoxyuridine, *EdU*, was used to stain replication sites of nascent DNA. The staining was performed without the use of antibodies, but thanks to a Click it reaction. Invitrogen™ EdU was incubated, 10 μM, in the cell's flask for 25 minutes at 37°. Then cells were plated and fixed with 10 minutes incubation of 4% paraformaldehyde (w/v), PFA at RT. Then, we washed two times with 3% BSA and we performed 20 minutes permeabilization with 0,5% Triton 100X. The EdU detection was performed with the Click-iT EdU imaging kit, by Thermo-Fisher Scientific, by using the Alexa axide 488.

All the sample prepared for this work were mounted overnight by using the Invitrogen ProLong Diamond Antifade Mounting Medium (P36965).

Experiments

All the acquisitions performed in this thesis were performed using a Nikon N-SIM Super-Resolution Microscope equipped with a 100x objective, with 1.49NA (CFI Apo TIRF 100xc Oil, Nikon) and with a grating block suitable for our multicolor experiments, the 3D EX V-R 100x/1.49.
The laser excitation was provided by a 4-laser unit equipped with 405nm, 488nm, 561nm and 640nm. Alexa 488 excitation was performed at 488nm and the emission was collected between 515-545nm. ATTO 594 was excited at 561nm and the emission was detected at 590-640nm.

DISCUSSION

In this work, we show that the spatial information encoded within SIM raw data can be quantitatively evaluated by using the SPLIT algorithm. This new SPLIT−SIM reconstruction method has interesting differences compared to most of the reconstruction algorithms used in SIM. Indeed, most of these are based on the OTF, which is a detection passband of the microscope corresponding to the Fourier Transform of the Point Spread Function. In these SIM algorithms each raw image of the stack is then used to access high frequency information, i.e. super-resolution features, to reconstruct the final image. The superimposition of the illumination frequency pattern onto the sample gives rise to the moiré fringes that, in the frequency domain, allow shifting of the high-resolution information within the diffraction limited detection passband, allowing features smaller than the diffraction limit to be resolved [111]. On the other side, our SPLIT-SIM algorithm exploits the intensity variation occurring in each pixel due to the phase variation of the excitation pattern. In particular, we demonstrated that fluorophores localized in the center of the PSF and fluorophores in the periphery show different fingerprints when considered in relation to the phase variation of the pattern. These fingerprints allow a super-resolution image to be generated by decomposing the intensity detected at each pixel. We investigated a potential application of the SPLIT-SIM algorithm, that is the study of chromatin organization and compaction

within the nucleus. In this context, SIM microscope has interesting features such as its low levels of illumination power to perform super-resolution acquisitions, and also its capability to perform multi-color imaging with conventional antibodies. For these reasons, SIM stands out among other super-resolution techniques in the study of chromatin organization at a maximum resolution of ~100nm [82, 112, 113]. In this context, we demonstrated that SPLIT-SIM is a simple tool able to generate super-resolution images of chromatin and other functional sites within intact cell nuclei. In particular, we showed that SPLIT-SIM is a valuable tool in generating super-resolution images bypassing the traditional Fourier reconstruction. Moreover, without deconvolution it can reach a comparable resolution in respect to our microscope reconstruction software.

We also showed that the Phasor plot can be useful, especially for unskilled users, to directly evaluate the quality of SIM raw data in the case of sparse particles. Moreover, our SPLIT-SIM algorithm can be used with any SIM setup and it is easy thanks to its user-friendly organization.

Until now, the SPLIT approach has only been applied and investigated in the context of STED microscopy. In this chapter we demonstrated, for the first time, the applicability of SPLIT to other super-resolution techniques. For this reason, we believe that SPLIT can be applied also to other super-resolution techniques such as image scanning microscopy, ISM [68], but also in the case of the combination of SIM with single molecule techniques, i.e. SIMFLUX [114] and SIMPLE [115].

Chapter 3

Analysis of multi-color structured illumination microscopy data by image cross-correlation spectroscopy

In the last decades, super-resolution (SR) techniques have been exploited in many biological studies, thanks to the possibility of reaching an unprecedented resolution to unveil the basis of fundamental cellular processes. Therefore, many biological projects aim at reaching not only a higher resolution but also more quantitative information about the relationship between different targets.
In microscopy, using multicolor labeling, it is possible to investigate and analyze the distribution of the molecules in each channel and the relative distribution of particles of different colors. To perform two-color analysis in microscopy acquisitions, the easiest approach consists of analyzing the overlap of the colors of both channels. The overlapping of the two colors in a pixel indicates the spatial co-localization of the target molecules at a given position in the cell environment.
Thus, in optical microscopy, the localization precision of molecules is strictly bound to the resolving power of the microscope. In conventional microscopy, when molecules of two different colors have a distance of 250nm or closer, they will be unresolved and will appear co-localized.
Thanks to the introduction of novel techniques, it has been possible to overcome this limitation, thus reaching a nanoscale resolution. One of these techniques is Proximity Ligation Assay, PLA, [116] in which two antibodies are functionalized with two different primer oligonucleotides. These two antibodies link to the target molecules, and if they are closer than ~40nm, then the oligonucleotides will be close enough to link to one another, creating a circular DNA molecule by amplification. This molecule will be recognized by additional functionalized probes and it will be detected thanks to its fluorescence signal. Another example, which reaches even higher resolution is Forster resonance energy transfer, FRET, [117,118] in which an excited ‘donor’ molecule interacts by energy transfer with an ‘acceptor’ fluorophore through a dipole-

dipole coupling. Accordingly, relying on this close interaction, this technique can only probe distances smaller than ~10nm. These two techniques opened the possibility to investigate molecules interactions in the range between ~2-40nm, leaving a gap from ~40nm to ~250nm.
In this context, the introduction of super-resolution techniques, changed dramatically the possibilities to investigate samples in the range from ~20nm to ~250nm [119,120].
All the available SR techniques, cited in chapter one, when coupled with the appropriate analysis tool can be used to perform precise localization or co-localization studies.

Main Goal of the Project

In this thesis work, one of our final goals was to investigate chromatin organization and its modifications in the presence of genetic mutations inducing pathology, but to address this question accurately we needed a ground truth on SIM co-localization analysis.
To quantify co-localization in two-color images there are two main approaches. The first one includes object-based methods [109], which foresee the segmentation of the acquired images into single objects. Each object is characterized by precise x, y, z coordinates allowing the analysis of the distribution of each single channel molecule and their relative spatial organization. Moreover, object-based methods allow the creation of a map of every single object in both channels, thus mapping also the co-localized particles. Considering that they are based on the use of a list of coordinates, object-based techniques are widely used in Single Molecule Localization Microscopy, SMLM, because the acquired raw data is already in a list of coordinates of every single molecule. However, they can be used with any microscope acquisitions, only after the segmentation of the images, and as long as the molecules, or more generally the target structures, are isolated and well resolved [121].

To summarize, object-based techniques allow performing a complete statistical analysis of the relative distribution of the molecule of interest and provides a localization map of the whole sample.

The second approach that can be used to analyze two-color measurements are the pixel-based methods. These techniques do not require pre-segmentation of the image into objects because they rely on the extraction of the correlation coefficient from each pixel intensity of the acquired image. Pixel-based methods can be applied to every microscopy data set, also when the particles are not well isolated and resolved, to quantify the relative distribution of multicolor-channel acquisitions. One method used to study dynamic interactions is Fluorescence Cross-Correlation spectroscopy (FCCS), which is a two-color version of Fluorescence Correlation Spectroscopy (FCS) [122]. In FCCS, the quantity of interacting particles is calculated by analyzing the temporal intensity fluctuations due to the variation of fluorophore concentrations within the observation volume [123,124]. Moreover, it has been demonstrated that the same formalism of FCS and FCCS can be used to analyze spatial intensity fluctuations in images. Therefore, Image Correlation Spectroscopy, ICS, and Image Cross-Correlation Spectroscopy, ICCS, are the corresponding spatial versions of FCS and FCCS [125]. Image cross-correlation spectroscopy, ICCS can be used as a pixel-method to analyze spatial distribution of particles in images [126]. Moreover, ICCS has been already used in combination with SR techniques, giving interesting insights into biological co-localization analysis [127]. In this work, Dreier et al. demonstrated that from ICCS it is possible to extract an average distance value information in correlated samples, and also a map of co-localization. Nowadays, ICCS analysis has only been coupled with STED nanoscopy, and, to the best of our knowledge, still it has not been implemented with SIM.

Here we demonstrate that SIM can be coupled both with object-based techniques and with ICCS analysis and we investigate the efficiency of these methods to extract real distances in a fabricated model sample.

In the first part, we couple SIM with an object-based method, then we focus on SIM-ICCS analysis. In both cases, we investigate its capability to extract the real distance on ‘SIM-nanorulers’, DNA-origami containing two-color fluorophores located at a well-defined distance. They comprehend one central

region labeled by green fluorophores lying precisely at 80nm distance between two regions labeled with red fluorophores.
We show results about SIM coupled both with an object-based method, and a pixel-based method, ICCS.

RESULTS

SIM imaging of optical nanorulers

To measure nanoscale distances in SIM acquisitions, we choose a two-color nanoruler, 160RBR from Gattaquant, which are fabricated with one central region labeled with a group of green fluorophore Alexa 488 spaced by 80nm from two red fluorescent molecules, ATTO 647N, as shown in figure 3.1. We choose these two colors because we planned to use them in biological specimen immunostaining. The first thing we did in this study was to check the achievable resolution of our microscope with these samples. To do so we performed a line profile analysis, as shown in figure 3.2, in which we plotted the nanometer distance in the x-axis, and the fluorescence intensity in the y axis. From the analysis of 15 different single nanorulers in each channel we estimate a ~140nm resolution in the green channel and a ~135nm resolution in the red channel.

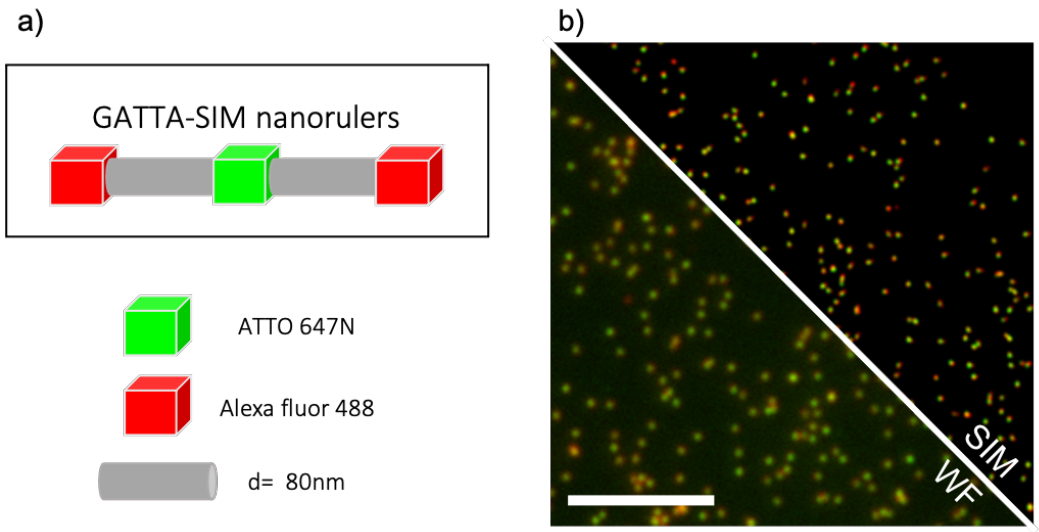

Figure 3.1. Nanoruler structure and image. **a)** Schematic representation of GATTA-SIM nanorulers. Each nanoruler presents two groups of red fluorophores at the ends, ATTO 647N, and one central group of Alexa fluor 488 green fluorophores spaced from the two red ones by 80nm. **b)** Comparison between Widefield and N-SIM reconstructed image of GATTA-SIM nanorulers, ROI 256x256 pixels, scalebar 5µm.

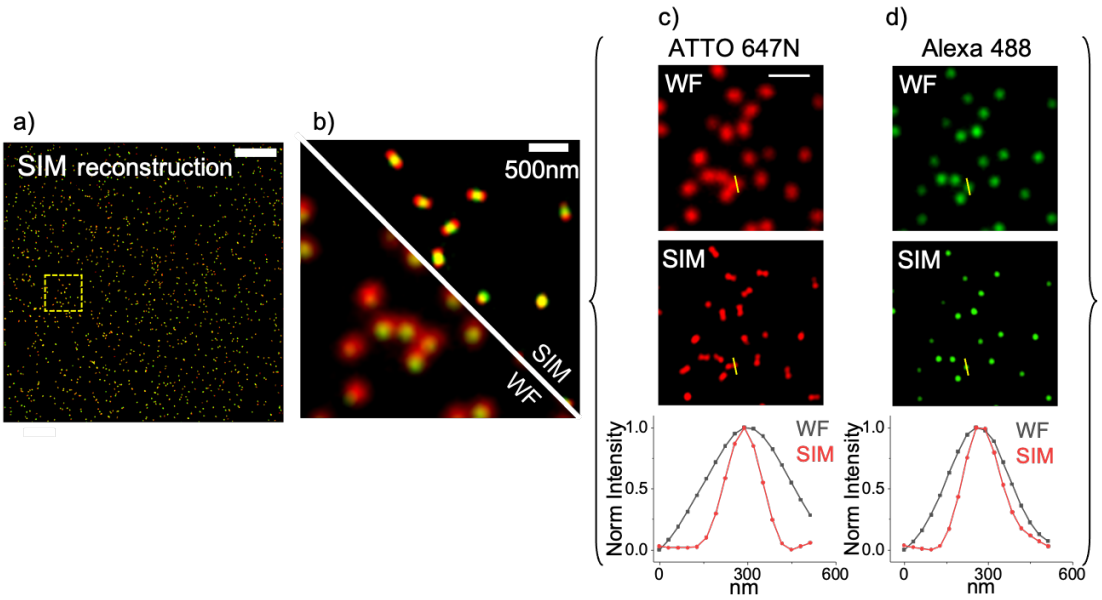

Figure 3.2. Line profile analysis on nanorulers images to evaluate the resolution achieved. a) 512x512 pixel SIM reconstructed Image, scale bar 5µm. **b)** 128x128 pixel ROI from image a). Shown are Widefield acquisition, bottom left, and SIM acquisition top right, scalebar 500nm. **c)** Red channel acquisitions, respectively on the top Widefield acquisition, in the middle SIM acquisition and the line profiles analysis of the nanoruler to define the resolution (r), signed with the yellow line in both WF and SIM images. r_{WFred} ~350nm; r_{SIMred} ~137nm. **d)** Green channel acquisitions, from top to bottom respectively Widefield, SIM acquisition, and line profile analysis highlighted with the yellow line in both WF and SIM images. $r_{WFgreen}$ ~260 nm; $r_{SIMgreen}$ ~150nm.

Measuring nanoscale distances by object-based analysis

The knowledge of our setup resolution allowed us to accurately perform the object-based analysis, by setting the minimum particle size recognizable at 128 nm, i.e. 4 pixels. We considered eleven acquisitions of nanorulers and we analyzed each single two-color image. Then we collect together all the distance information from all the acquisitions and we built a cumulative histogram.

The cumulative RDD, 'relative distribution distances' graph, in figure 3.3, shows a co-localization peak (fluorophores in the same nanoruler) superimposed to a linear growing component, red dashed line, which corresponds to random distances, i.e. non-co-localized molecules (fluorophores in different nanorulers). We subtract the random distribution distances from the cumulative RDD histogram, as shown in figure 3.3f, and we consider only the co-localization peak to perform a Gaussian fit to extract an average distance value. We found that the mean distance was d_{obj}= 76 ± 20

nm (mean ± SD) which is in agreement with the expected real value d_{real}=80nm.

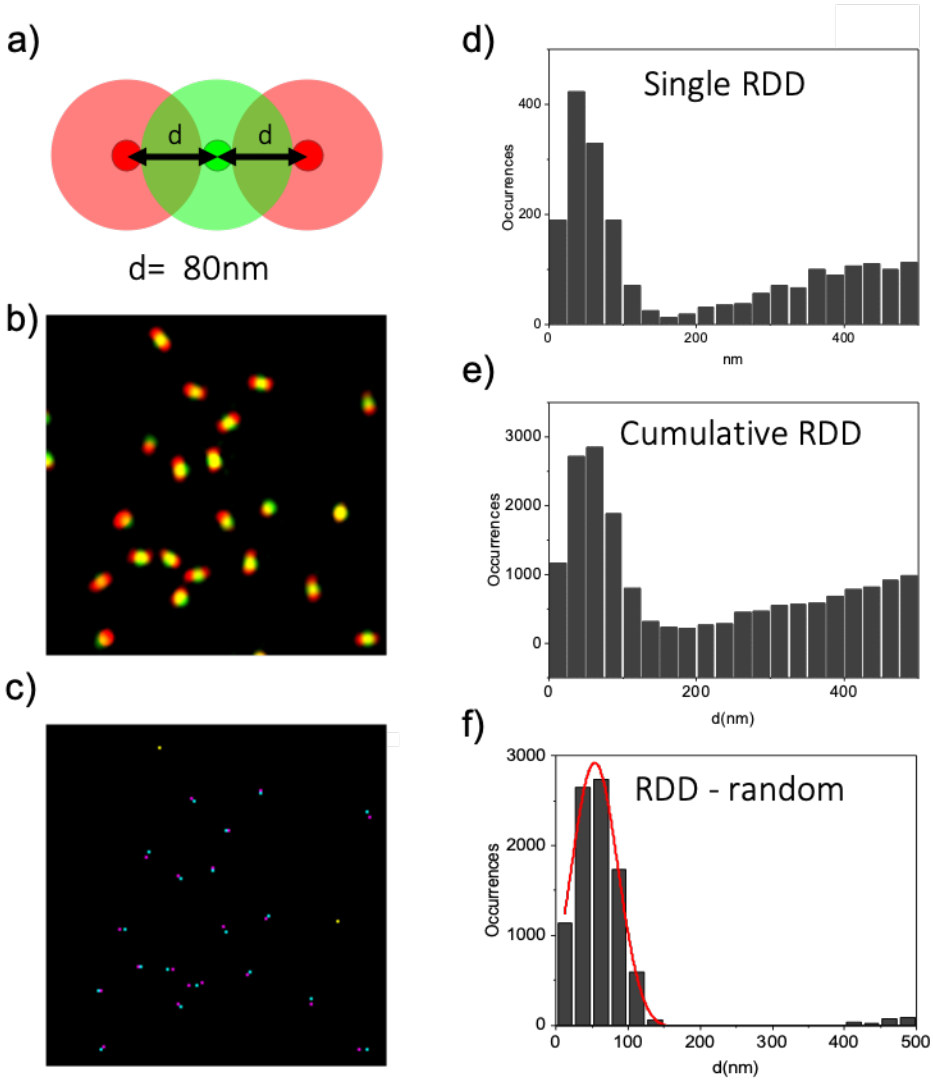

Figure 3.3. Object based analysis on nanorulers. a) Schematic representation of GATTA-SIM nanoruler PSF. **b)** 128x128 pixels ROI of SIM reconstructed super-resolution image. **c)** Map of the center of mass defined by the Object-based analysis. Magenta and Cyan spots indicate molecules in the red and green channel respectively, whose distance is 30nm< d <160nm, whilst the yellow spots indicate structure whose center of mass is closer than 30nm, which corresponds to our pixel size. **d)** Relative distribution distances, RDD, histogram of a single 512x512 reconstructed image. **e)** Cumulative RDD histogram of eleven samples considered in the analysis. **f)** Gaussian fit of the RDD histogram without the random component. The analysis of the co-localization peak in all the eleven samples gave a mean distance of d= 76 ± 20 nm (Mean ± SD).

In summary, object-based analysis allows a complete statistical analysis of all the distances calculated in a two-color image. It shows a co-localization map of all the detected center of mass, and it provides the user with a list of coordinates and distances of all the molecules considered.

Measuring nanoscale distances by SIM-ICCS analysis

At this point, we moved to super-resolved ICCS analysis. In ICCS the colocalization fraction f can be calculated from the amplitude of the cross-correlation function [107, 122]. Recently, Oneto et al showed that the shape of the cross-correlation function is strictly linked to the average distance, *d*, between correlated molecules and to the spatial resolution of the microscope [107]. In particular, when two molecules are separated by *d* in one direction, their two-dimensional auto-correlation functions have width w_{11} and w_{22}. Instead, their relative 2D cross-correlation function, w_{cc}, will be shifted from the origin of a distance *d*, and it will be $w_{c-c} = [(w_{11}^2 + w_{22}^2)/2]^{1/2}$. In real samples, the two sets of molecules can be oriented in multiple directions in respect to each other and the cross-correlation function will be affected by this, and it will have a decreased amplitude value and an increased width value. This enlargement is calculated as $\Delta w = w_{12} - w_{c-c}$ with Δw that depends only on the average distance of the correlated particles.

We performed SIM-ICCS analysis on the 11 samples used for the object-based analysis, previously shown in figure 3.3. As expected, we obtained a positive cross-correlation function for each two-color image, as shown in figure 3.4b). We calculated the average value of all the cross-correlation functions and the result was f_{ICCS}= 1,11 ± 0,51 (mean ± SD). The ICCS algorithm calculates the width of each cross-correlation function and extracts the distance, thus we calculated the distance value in all the eleven samples, as shown in figure 3.4c). Then, we calculated the mean distance value as d_{ICCS}= 80 ± 9 nm, in agreement with the real distance d_{real}= 80nm.

In summary, we show that SIM-ICCS gives information about the average distance between correlated particles.

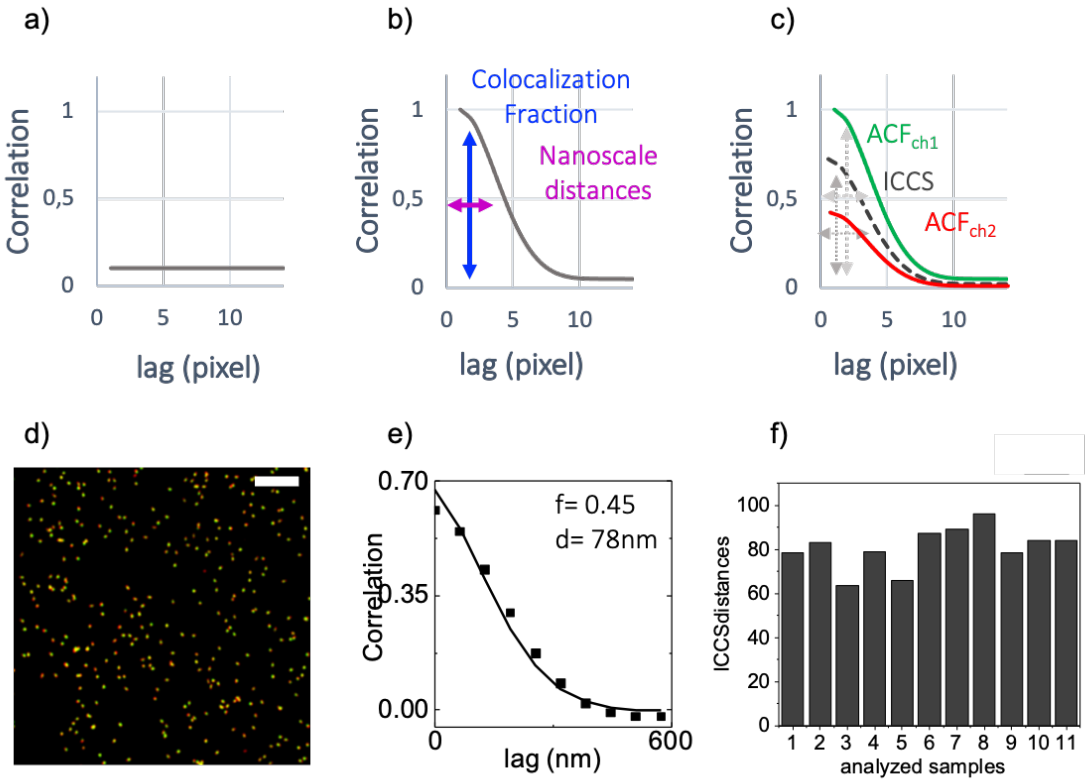

Figure 3.4. ICCS Analysis Results a) Schematic of the Cross-Correlation Function, CCF, of non-co-localizing sample **b)** CCF of co-localizing sample from which FWHM can be extracted nanoscale distances, and from CCF amplitude can be evaluate the colocalization fraction. **c)** scheme of the auto correlation functions, ACFs, in red and green, from two-color sample and their relative CCF, in dashed grey. d) SIM reconstructed super-resolution image, 512x512 pixel ROI. Scalebar 5µm. **e)** Single two-color image cross-correlation function. Cross-correlation function value (f) and characteristic sample distance (d) are shown in panel b. **f)** Histogram of ICCS distance values found in each single 11 samples analyzed, from which we calculated the average distance d = 80 ± 9 nm (Mean ± SD).

MATERIALS AND METHODS

Data analysis

Object-based analysis

The object-based analysis was performed using an ImageJ plugin called JACoP [109], following the procedure presented in Oneto et al. [107]. This plugin works only with two-color images and first requires manual setting of the threshold to select the particles that will be considered in each channel.

The second step of calibration requires knowledge of the image pixel size, then the algorithm needs to know which wavelength was used, the Numerical Aperture of the objective, and the refractive index of the oil used. In the last step before the actual analysis, we can choose the minimum particle size. In our microscope the pixel size is 33 nm^2 and the calculated resolution in this sample was ~135nm, therefore, we set the minimum particle size at 4pixels. After this accurate calibration, the plugin performs the analysis and then provides a set of data including the x, y, z coordinates for each particle in each channel and the value of distances between each molecule of the first channel from all the particles of the second channel. In this plugin, particles are considered colocalized when their distance was smaller than ~164nm. We used the list of distances provided by JACoP to build a histogram in which we plot the distribution of the distances on the x-axis in relation to the occurrences on the y axis. Here, we refer this histogram as "relative distance distribution" (RDD) graph. The random component of the histogram (i.e. the contribution of non-correlated particles), was calculated using a linear fit forced through the origin in a distance range of 250nm to 500nm. The calculated random component, RC, was then subtracted from the cumulative data, RDD, obtaining the colocalization peak without the random component. The RDD – RC graph was used to perform a Gaussian fit, from which we extracted the average distance value found with this analysis.

Image Cross-Correlation Spectroscopy (ICCS) analysis

Image correlation spectroscopy (ICS) and Image cross-correlation spectroscopy (ICCS) analysis were performed in Matlab using the open-source algorithm described in Oneto et al. [107] ICS algorithm was used to evaluate the resolution achievable in the images, while spatial autocorrelation functions, ACF, were used to find the Full Width at Half Maximum (FWHM) from which we extracted the average distance value.

In particular, ICCS 2D image correlation functions were calculated as

(1)

$$G_{ij}(\delta_x, \delta_y) = \frac{< I_i(x,y) I_j(x+\delta_x, y+\delta_y) >}{< I_i(x,y) >< I_j(x,y) >} - 1$$

Where the angle brackets indicate the average of all the pixels from the image, and $I_1(x,y)$ and $I_2(x,y)$ correspond to the images in the two-channels. To calculate the Auto Correlation Functions, ACF, we set i=j=1 and i=j=2. Whilst, to calculate the Cross Correlation Function, we set i=1 and j=2. The numerator in equation, $I_i(x,y)I_j(x+\delta_x, y+\delta_y)$, was calculated thanks to a fast 2D Fourier transform algorithm. Next, the 2D correlation functions were converted into one-dimensional radial correlation functions, $G_{ij}(\delta_r)$ by performing an angular mean as explained in Scipioni et. Al [128]. Finally, we performed a Gaussian fit of the calculated radial 1D correlation functions to find the values of the amplitude, $G_{ij}(0)$, and the width parameters, w_{ij}^2, as follows

(2)

$$G_{ij}(\delta_r) = G_\infty + G_{ij}(0)exp\left(-\delta_r^2/w_{ij}^2\right)$$

The width parameter corresponds to the $1/e^2$ of a Gaussian function and it is related to the FWHM by the relationship $w = FWHM/(2ln2)^{1/2}$. To calculate the co-localization coefficients M_1 and M_2

we used the amplitude parameter: $M_1 = \frac{G_{12}(0)}{G_{22}(0)}$ and $M_2 = \frac{G_{12}(0)}{G_{11}(0)}$.

To calculate the co-localized fraction f_{ICCS} we performed the arithmetic average of the M_1 and M_2 coefficients.

The cross-correlation function broadening in respect to the relative autocorrelation function was evaluated as $\Delta w = w_{12} - w_{cc}$ with $w_{cc} = ((w_{11}^2 + w_{22}^2)/2)^{1/2}$. The Δw value was used to calculate a distance value $d_{ICCS} = \left(\frac{\Delta w}{C}\right)^{1/2}$ as explained in Oneto et al [107].

Sample

The sample used to perform this analysis study was a GATTA-SIM Nanoruler 160RBR purchased from Gattaquant DNA Nanotechnologies. Every single nanoruler is fabricated with three group of fluorophores, ATTO 647N - Alexa Fluor® 488 - ATTO 647N, spaced 80nm apart from each other. The disposition of these nanorulers is not always parallel to the glass surface due to their immersion in the mounting medium. The non-parallel nanorulers will influence the distances analysis both with ICCS and Object-based methods.

DISCUSSION

In chapter 3, we showed that SIM-ICCS is a powerful tool to accurately investigate colocalization events. We validated SIM-ICCS results by using a model sample and by comparing the technique with another co-localization analysis method, based on objects.

The object-based techniques showed some limitations when the single objects were not well isolated and/or resolved. Indeed, in the red channel, there are two group of particles outdistanced of 160nm and our microscope resolution was 135nm. In this case, setting a lower threshold means not separating properly the two structures of each red nanoruler. Accordingly, the JACoP plugin sets the center of mass in the middle between the two poorly resolved red fluorophores. An inaccurate selection of the center of mass occurs in the majority of the structures present in an image, will lead to a wrong estimation of the average distance in the sample. For example, in our nanoruler this would have meant setting the center of mass of the two-red fluorophore in the middle between the two, very close to the position of the green fluorophore. In this way, the colocalization peak will not give a correct estimation of the distance ~80nm, but it would have been smaller. To avoid the incorrect estimation of distances in object-based analysis, we decided to sacrifice some of the structures in our sample and setting a higher threshold in the JACoP plugin. The higher threshold allowed the isolation of most nanorulers, which was fundamental in the accurate measurement of the distances. However, this higher threshold excluded from the analysis many low intensity nanorulers, decreasing the total number of calculated distances.

In this context, we found that the correct localization of every single center of mass was a limitation of the object-based analysis, in comparison with the ICCS. In fact, ICCS does not require the target structures to be well-resolved because it does not need the pre-segmentation of the image into objects.

In summary, this tells us that ICCS will be more suitable in co-localization analysis involving high-density samples because an object-based analysis would find less center of mass and thus be less accurate.

Another aspect brought up from this comparison is that, in a crowded isolated specimen, the computational time required to perform the complete analysis is the same as in ICCS analysis, because it relies only on the number of pixels. Whilst, in the object-based analysis, the computational time will be much slower because it relies on the number of objects detected.

Moreover, another aspect to be considered is that with the ICCS analysis, the correlation function shows if there is co-localization in the two-color sample, but it does not tell us anything about where the co-localization occurs. On the other hand, the object-based analysis provides a co-localization map with different colors to map co-localized or non-co-localized molecules. In particular it shows in yellow 'highly' co-localizing molecules where two structures are close ~10nm, in blue and magenta it shows co-localizing particle in the range of ~10-140nm, and in green and red it shows non-co-localizing particles, i.e. particles whose distance is >140nm.

However, Oneto et al. demonstrated that ICCS analysis can give information about the distribution of the co-localization events by creating a correlation map from the information obtained with the cross-correlation function calculated in small regions around each pixel. We believe that the same data can be extracted also from SIM-ICCS data, but we did not perform this 'map' step because nanorulers are homogeneously sparse in all the fields of the image.

The last aspect that emerged from this study is that the object-based analysis output data allows a complete statistical analysis of all the relative distances in the samples RDD histogram. Instead, in the ICCS approach, we cannot perform a complete statistical analysis, but we use the broadening of the correlation function to extract an average value of the distance between two color particles.

In conclusion, we have shown and demonstrated that ICCS is a powerful tool also when it is coupled with SIM measurements. Indeed, SIM-ICCS allows investigating the spatial organization and relative distribution of two-color acquisition and also allows studying crowded samples giving accurate results.

CHAPTER 4

SIM-ICCS applied to biological imaging

In chapter 3 we demonstrated that it is possible to perform accurate two-color analysis on SIM reconstructed data through ICCS analysis, and we compared and validated the results with an object-based approach. Indeed, we believe that SIM-ICCS can be an interesting tool in the investigation of biological problems. In particular, the final goal of our research is to understand how alterations in the organization of the genomic information can affect the healthy state of a eukaryotic cell.

In the last decades, it has been highlighted that there is a connection between chromatin structure and cell's fundamental functions [129]. Unveiling this relation can help in understanding disease occurrence and, consequently, how to develop pharmaceutical treatments. In healthy eukaryotic cells, fundamental processes need to be well regulated and spatio-temporarily coordinated to perform their function properly [130]. On the contrary, in tumoral cells, they are often unregulated, and spatio-temporarily unsegregated. This leads to the simultaneous occurrence of these processes, causing competition against each other, leading to DNA damage [131]. This DNA damage causes genomic instability which is one of the main hallmarks of cancer and is associated with an increased possibility to generate and accumulate DNA damage [132]. Recently it has been proposed that alterations in oncogenes expression can be responsible for the activation of molecular events, causing genomic instability leading to tumorigenesis. However, cancer development and its related molecular mechanisms are almost unknown. One of the formulated hypotheses is that the altered expression of oncogenes can induce DNA damage by influencing fundamental processes such as DNA replication. It has been proposed that this so-called, 'replication stress' [133] can be caused by interference between the DNA replication process itself and DNA transcription [134]. To address these studies, multiple genomic techniques were introduced which enabled the study of single genes and regulatory elements of the whole genome [135].

In this context, genomic sequencing was fundamental in generating information about cell developmental stages and the analysis of genetic variations. Functional genomic techniques allowed the characterization of each regulatory sequence's role in human disease [136]. Every genomic technique was fundamental in unveiling these aspects of the genomic heritage, and reaching a high-resolution in defining spatio-temporal regulation of each genomic function.

However, every genomic approach misses information related to the spatial organization and spatial localization of genetic processes within single cells. This information can be explored thanks to the use of Super-Resolution optical microscopy.

Main goal of the project

The main goal of this project is to develop a quantitative technique to evaluate oncogene-induced alterations in chromatin organization by using as a SR technique Structured Illumination Microscopy. The main idea behind this work is that the altered expression of oncogenes can influence the spatio-temporal organization of DNA transcription and replication. One of the proposed events that can happen at the early tumorigenesis is that replication and transcription machineries are not spatio-temporarily coordinated, thus compete with each other on the same DNA strand. This competition can cause the physical collision of the two machineries causing DNA damage and genomic instability. In practice, we would like to verify if these collisions occur, by studying eventual alterations in the spatial distribution of replication and transcription foci after the activation of an oncogene. We will then analyze SIM data by SIM-ICCS and object-based methods to verify whether there are any co-localization events. Our aim is to apply our analysis on characteristic biological samples. In particular we will use an in vitro cell model in which it is possible to selectively activate oncogene expression. One of this cell lines is the MCF-7 model cell line that comes from a patient suffering from breast adenocarcinoma and is an adherent cell line. The other cell line, PR9-U937,

comes from Acute Promyelocitic Leukemia, APL, patients and is cultured in suspension.

In our work we will focus our attention to the SIM-ICCS analysis methods, which we will validate by comparing the results with an object-based technique. To perform the analysis, we will prepare different immunostaining on untreated cells. In particular, we will prepare a positive control that consists of a two-color stained sample in which the target nuclear structures show a co-localized distribution, and a negative control in which we labeled non-co-localizing nuclear structures.

RESULTS

Application of SIM-ICCS to biological imaging

In this work, we decided to use two particular cell lines engineered in which is possible to activate the expression of oncogenes. These cells are MCF7 with an inducible c-MYC allele and PR9-U937, that is a monoblastic cell line in which it is possible to induce the expression of a fusion protein PML/RARα.

In the MCF-7 cell line it is possible to induce the ectopic expression of the proto-oncogene c-MYC [137]. This c-MYC proto-oncogene became of interest in the last decades because it is often activated in human cancer. Even if its roles remain unclear, it is known that c-MYC is strictly linked to cellular proliferation and metabolic processes involved in cellular ‘metabolic transformation’ [138, 139]. The metabolic transformation typical in cancer disease is called the Warburg effect and it comprehends reduced oxidative phosphorylation, an increment in lactate production and glucose consumption [140]. Since the 1970’s the main theory was that the Warburg effect was caused by some mutations that induce cancer development. But recently it has been demonstrated that the fundamental elements in this ‘metabolic transformation’ are oncogenes. Among these, the overexpression of c-MYC oncogene is responsible for the majority of changes inducing malignant transformation of cells. Another reason why c-MYC is so interesting in cancer studies is that while it induces rapid cell division, it also inhibits the expression

of antiproliferative genes thus helping the tumor to grow uncontrollably. We choose this engineered cell line because we can exploit the possibility to study the same scenario both in 'normal' MCF-7 cells, with the physiological expression of the c-MYC oncogene, and in the 'activated' cells in which we induce the overexpression of the c-MYC oncogene by performing a Doxycycline, DOX, treatment as shown in figure 4.1.

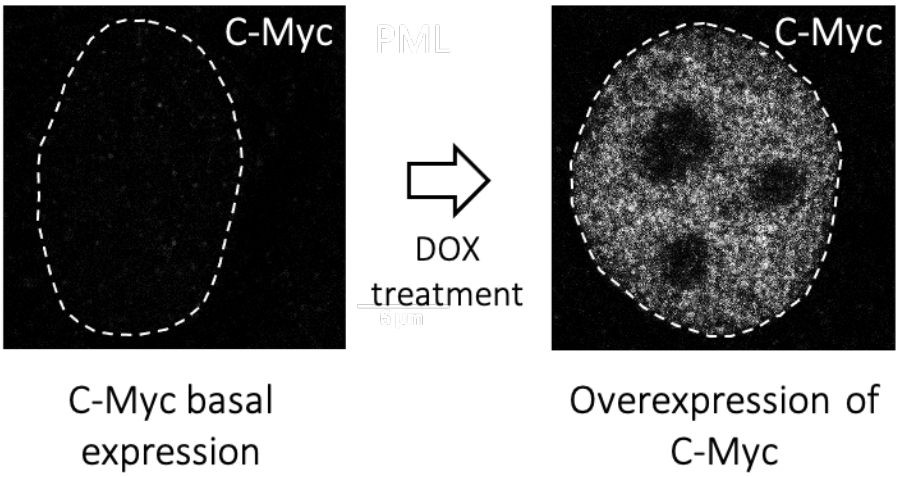

Figure 4.1. c-MYC stained to evaluate its activation. On the left, it is possible to see c-MYC basal expression in untreated cells. On the right, upon Doxycycline, DOX, treatment, it is possible to see c-MYC overexpression. (Image credit Dr. Elena Cerutti, IIT).

In the PR9-U937 cell line it is possible to induce the expression of the PML/RARα fusion protein. This fusion protein is present in most Acute Promyelocytic Leukemia patients. In this pathology the mutation of the RAR protein in the PML/RARα protein causes the interruption of the functions of the retinoic acid receptor, RARα. Instead, this mutation recruits many histones deacetylases, HDAC, complexes that are nuclear corepressors. This causes an inaccessibility to the DNA strand causing limitations in DNA transcription, replication and repair. Thus, the expression of PML/RARα causes a block in the maturation of cells that cannot grow over the promyelocytic stage [141, 142, 143]. To simulate these events the U937 cell line is transfected with the PML/RARα gene whose expression is controlled by a zinc-inducible promoter. Consequently, upon a zinc treatment, we will have the expression of the PML/RARα fusion protein as shown in fig 4.2.

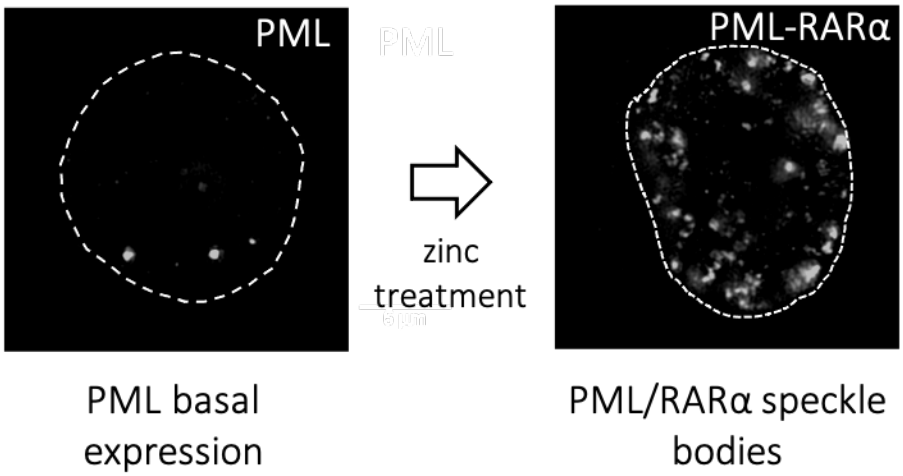

Figure 4.2. PML bodies stained to evaluate the expression of the fusion protein PML/RARα. On the left, it is possible to see the untreated cell with the PML bodies stained. On the right, upon 8H zinc treatment, ($ZnSO_4$ 1M solution), it is possible to see the disruption of PML bodies and the irregular expression of the PML/RARα fusion protein.

MCF-7 model Data analysis

In MCF-7 cells we performed the immunostaining for both the positive control and the negative control as explained in the methods section, and we acquired multiple cells to perform statistical analysis. In the positive control cells, we labeled Proliferating cell nuclear antigen, PCNA, which is a processivity factor that assists the work of DNA polymerase delta in the process replication of eukaryotic cells and 5-ethynyl-2'-deoxyuridine, EdU, which is a thymidine analog incorporated in the nascent DNA of replicating cells. We acquired 15 images and used both object-based analysis and pixel-based analysis.

In MCF-7 cells, from the object-based analysis, we found a co-localization peak and its Gaussian fit allowed defining the FWHM of the peak of 80 ± 4 nm (mean ± SD).

The SIM-ICCS analysis was performed on every single two-color image and then we calculated the mean distance, *d*, and the mean value of the cross-correlation function, *f*. In MCF-7 from SIM-ICCS we obtained a similar result when compared to the object-based analysis, finding a distance of 60 ± 5 nm (mean ± SD). Moreover, we calculated the mean value of the cross-correlation

function obtained in all the samples which was f= 0,61 ± 0,13 (mean ± SD). MCF-7 results are shown in figure 4.3.

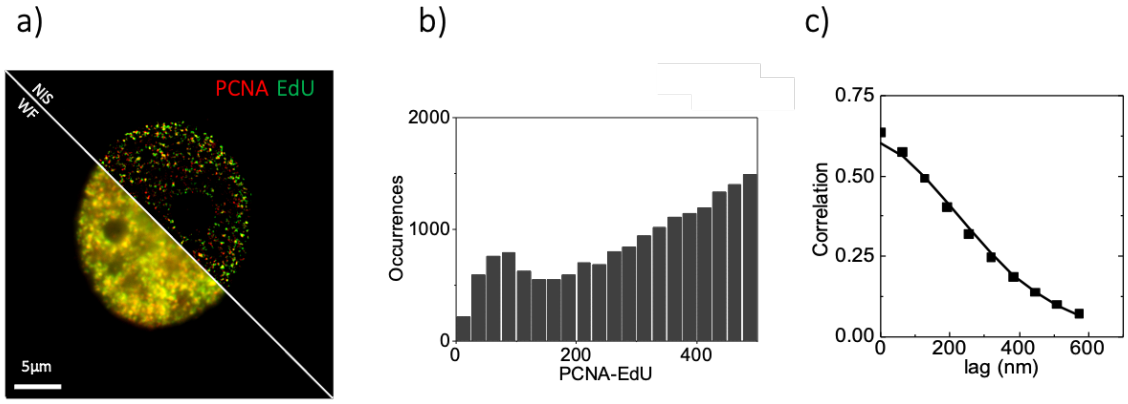

Figure 4.3. MCF-7 model Positive control immunostaining and analysis. **a)** 512x512 Image comparison between widefield, bottom left, and reconstructed data, top right, of the positive control sample, PCNA-EdU. Scale bar 5µm. **b)** cumulative relative distribution distances, RDD, histogram of all the samples considered for the analysis with a colocalization peak around 80nm superimposed to the random component. **c)** Positive cross-correlation function of the reconstructed image shown in (a) which tells us that SIM-ICCS analysis found co-localization within the sample.

Next, we prepared the negative control sample in which we stained elongating RNA polymerases phosphorylated at serine 2 (RNApol2ser2) which is a marker of active transcription, and histone H3 di-methylated at the 9th lysine, H3K9me2, which is associated with transcriptional repression, see methods.

We performed object-based and pixel-based analysis on 15 negative control samples. As expected, in the object-based analysis, we did not find any co-localization peak, indicating that the two nuclear markers do not have correlated spatial distribution. Moreover, the pixel-based analysis did not find any correlation, the mean value of the cross-correlation function was f=0, and with a zero value of the cross-correlation function, the algorithm cannot calculate a distance value. The results obtained from the negative control sample are shown in figure 4.4.

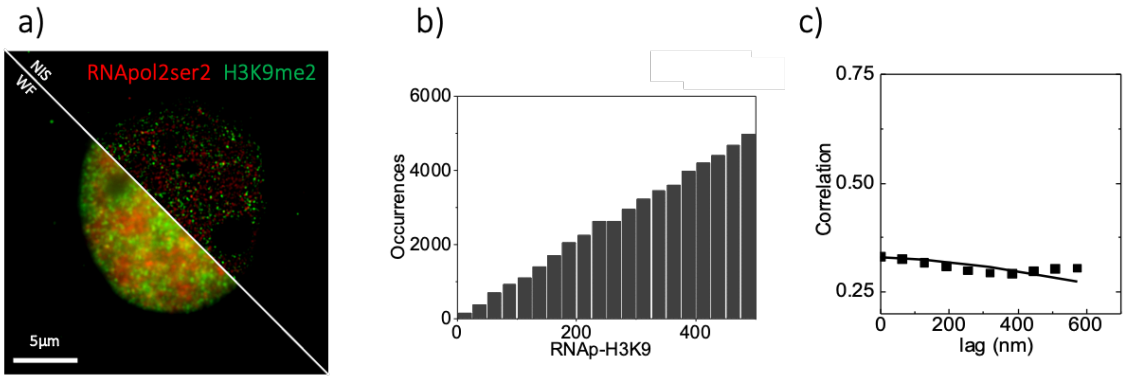

Figure 4.4 MCF-7 model Negative control immunostaining and analysis. **a)** Image comparison between widefield and reconstructed data of the negative control sample, RNApol2ser2- H3K9me2. **b)** object-based analysis representation of cumulative relative distribution distances, RDD, histogram of the samples considered. No evident co-localization peak means no colocalization in the samples. **c)** cross-correlation function of the reconstructed image shown in (a) shows that there is no correlation between the two-channel image.

In every biological analysis performed in this thesis work, we stained DNA by using Hoechst to have a nucleus counterstain and to discard apoptotic or unhealthy cells, as shown in figure 4.5. Two colors are necessary to perform the analysis in the test sample and both in positive and negative controls. The fourth color will be necessary to evaluate whether the treatment to induce the oncogene took place, thus it is fundamental to select the target cells.

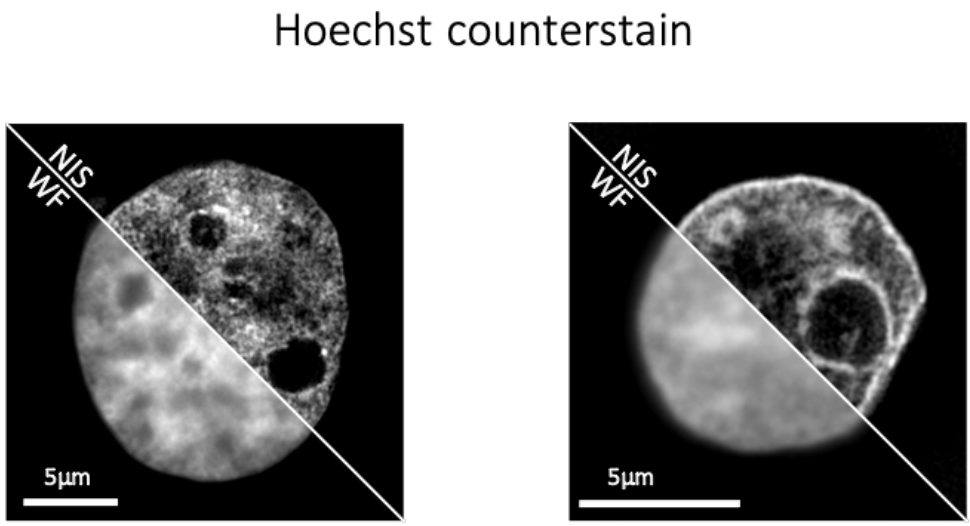

Figure 4.5 Hoechst counterstain. On the left, MCF-7 model stained with Hoechst both in WF and NIS elements acquisitions. On the right, WF and NIS elements acquisitions of PR9-U937M cell line. Scalebar 5µm.

PR9-U937 Data Analysis

As introduced previously, we also used another engineered cell line, PR9-U937, and we performed the object-based analysis on the positive and negative control.

For the positive and the negative control, we performed the same object-based analysis finding a co-localization peak. Again, we performed a Gaussian fit of the RDD histogram subtracting the random component and we found the FWHM of the co-localization peak around 121 ± 32 nm (mean ± SD) and the mean value of the correlation function was f= 0,69 ± 0,09 (mean ± SD). We calculated also the mean value of the distance, d, as 112 ± 16 nm (mean ± SD). Also in this cell line, both the object-based and ICCS analysis confirmed the correlated distributions of the two replication markers. PR9-U937 positive control results are shown in figure 4.3.

We tested also the negative control and, as expected, in the object-based analysis we did not find any co-localization peak, indicating that the two nuclear markers are randomly distributed among each other.

In the ICCS algorithm, we set f_{ICCS}=0 when we have CCF fits with the χ^2 value 50 times larger than the χ^2value of the ACF fit or when fits show a CCF width w_{12} too different from the average of the auto correlation functions width ($r_w < 0{,}5$ or $r_w > 2$ considering that $r_w = w_{12}/(w_{11}w_{22})^{1/2}$or when fits had a negative offsets $G_\infty (G_\infty < -0.2G_{12}(0))$.

For this reason, in the negative sample, the average d value of each image analyzed with the pixel-based analysis, ICCS, was f=0. In this case, the algorithm does not calculate a distance value. Results obtained from the PR9-U937 negative control sample are shown in figure 4.6.

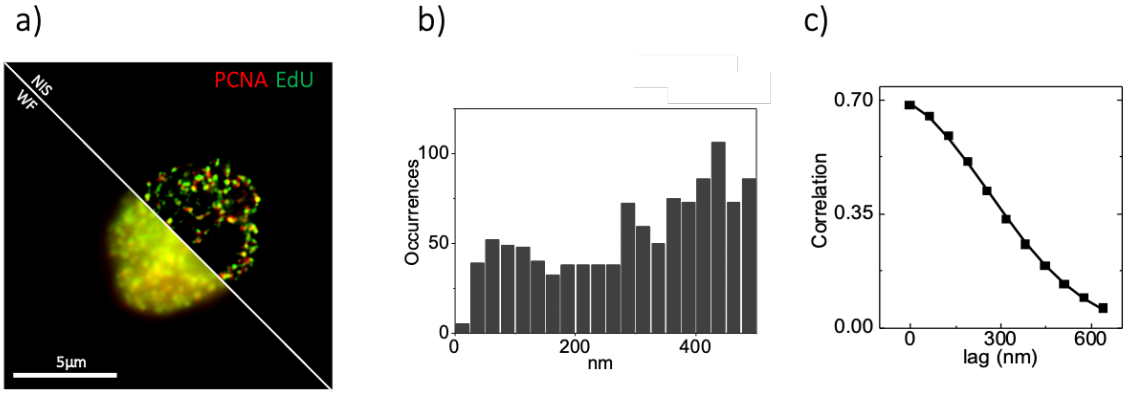

Figure 4.6. PR9-U937 Positive control immunostaining and analysis. **a)** 256x256 widefield and reconstructed data of a positive control sample, PCNA-EdU. Scale bar 5µm **b)** RDD histogram of samples considered with a colocalization peak around 90nm. **c)** Positive cross-correlation function of the reconstructed image shown in (a) which tells us that SIM-ICCS analysis finds co-localization in the sample.

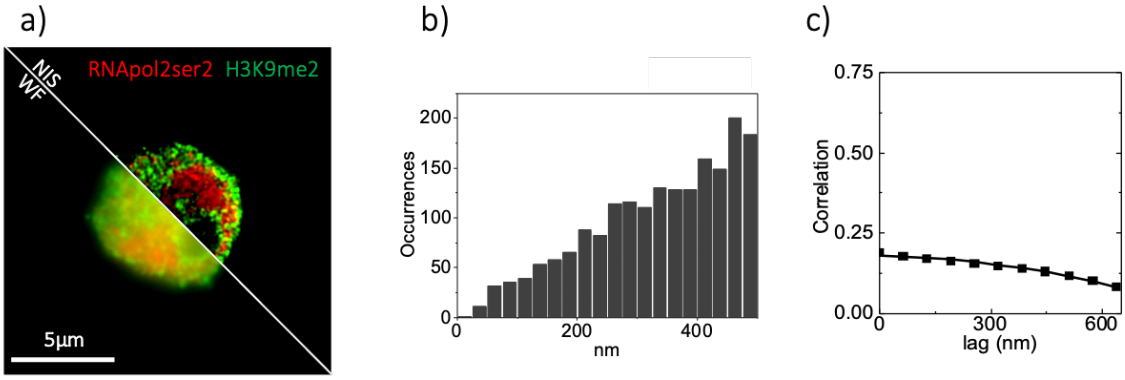

Figure 4.7. PR9-U937 Negative control immunostaining and analysis. **a)** 256x256 widefield and reconstructed data of the negative control sample, RNApol2ser2- H3K9me2. **b)** object-based analysis RDD representation **c)** cross-correlation function of the reconstructed image shown in (a) show that there is no correlation between the two-channel image.

MATERIALS AND METHODS

Samples

In this work we used MCF-7 model cell line that were grown in Dulbecco's modified Eagle's medium (DMEM) (Sigma Aldrich) integrated with 10% Fetal Bovine Serum (Euroclone ECS0180L) and 1% penicillin/streptomycin (Sigma Aldrich). Moreover, we used PR9-U937 cells that were grown in Roswell Park Memorial Institute medium (RPMI-1640 medium from Sigma Aldrich)

supplemented with 10% Fetal Bovine Serum (Euroclone ECS0180L) and 1% penicillin/streptomycin (Sigma Aldrich). For each line, Cells were grown in their flasks and then transferred to 14mm glass coverslips 1.5 high precision for imaging and fixed with 4% paraformaldehyde (w/v), PFA, fixation at RT for 10 minutes.

Immunostaining

The *Proliferating Cell Nuclear Antigen*, PCNA, the RNA polymerases, RNApol2ser2, and the Histone H3K9me2 were performed after 1-hour Blocking Buffer (BB) solution incubation at RT. The BB solution consists of 3% Sigma Aldrich Bovine Serum Albumin (BSA) and 0,5% Triton 100X.

The *PCNA* staining was performed overnight at 4° Celsius, by using a dilution [1:2000] of primary antibody Rat anti-PCNA by Chromotek (16D10) in the BB. The next morning the sample was washed once in BB solution and twice in the Washing Buffer solution (WB), which is made by 0,2% BSA and 0,06% Triton 100X. The cells were then incubated with the secondary antibody for 1-hour, which was anti-rat ATTO 594 [1:500] dilution in BB, then it was washed once in BB, twice in WB and three times in Phosphate Buffered Saline, PBS, solution.

The *RNA polymerases*, RNApol2ser2, which is a marker of elongating DNA, was stained with an 4° Celsius overnight incubation with an Abcam rabbit anti-RNApol2ser2 (ab5095), in a [1:500] dilution. Then cells were washed once in BB and twice in WB. Next, cells were incubated for 1-hour at RT with the secondary antibody anti-rabbit ATTO 594 in BB [1:500]. The last washing step was performed as previously described for the PCNA staining.

The last immunostaining concerning the *histone H3K9me2*, and was performed after a 1-hour BB incubation, and by incubating the primary antibody, Abcam mouse anti-H3K9me2 (ab1220), overnight at 4° Celsius. Next, the sample was washed once in BB and twice in WB, then it was incubated for 1-hout with the secondary antibody, anti-mouse Alexa 488, [1:1000] dilution. Then it was washed once in BB, twice in WB and thrice in PBS.

The 5-*ethynyl-2'-deoxyuridine*, EdU, was used to stain replication sites of nascent DNA. The staining was performed without the use of antibodies, but by using a Click it reaction. Invitrogen™ EdU was incubated, 10 μM, in the cell's flask for 25 minutes at 37° Celsius. Then cells were plated and fixed with a 10 minutes incubation of 4% paraformaldehyde (w/v), PFA at RT. Then, we washed two times with 3% BSA and we performed a 20 minutes permeabilization with 0,5% Triton 100X. The EdU detection was performed with the Click-iT EdU imaging kit by Thermo-Fisher Scientific, using the Alexa axide 488.

In all the samples prepared for this work we counterstained DNA by using Hoechst (Thermofisher 33342) diluted [1:4000].

Then, all the samples prepared for this work were mounted overnight by using the Invitrogen ProLong Diamond Antifade Mounting Medium (P36965).

Experiments

All the acquisitions performed in this chapter were performed using a Nikon N-SIM Super-Resolution Microscope equipped with a 100x objective, with 1.49NA (CFI Apo TIRF 100xc Oil, Nikon) and with the 3D EX V-R 100x/1.49 Grating Block. The laser excitation was provided by a 4-laser unit equipped with 405nm, 488nm, 561nm and 640nm. Hoechst was excited at 405, and was detected from 440nm to 485nm. Alexa 488 excitation was performed at 488nm and the emission was collected between 515-545nm. ATTO 594 was excited at 561 and the emission was detected at 590-640nm. ATTO 647N was excited at 640nm and its emission collected between 665nm and 738nm due to the filters mounted on our microscope.

DISCUSSION

In this last chapter of my Ph.D thesis, I showed that SIM-ICCS can be a powerful tool to evaluate colocalization events in two-color biological acquisitions. We validated its consistency by comparing the results with an object-based analysis method and by performing co-localizing and non-co-localizing immunostaining. As discussed in chapter 3, the object-based technique showed a limitation when the structures in an image are not well resolved. In the biological application, we found this limitation mainly in the PR9-U937 cell line. This cell line, as shown in figures 4.6 and 4.7, has smaller dimensions compared to MCF-7 cell line, thus the nucleus is more crowded. When structures are too crowded the object-based analysis will be less precise, and on top of that, SIM is not at its best performance in these labeling conditions. As with the nanorulers analysis, we used a higher threshold to perform the analysis of biological structures, 'leaving' behind some of them. These limitations, in the case of biological samples, make SIM-ICCS our preferred analysis technique. We plan to exploit SIM-ICCS's full potential by performing the local analysis on the biological samples to deeper investigate where the co-localization events occur within cell nuclei.

Another aspect of the comparison of these two techniques on biological samples is the computational time required. In the object-based method, the time needed to perform the complete analysis is more in respect to ICCS. This is due to the segmentation step needed and also because of the amount of coordinates data, which depends on the number of objects found.
In conclusion, we have demonstrated that ICCS can be a powerful analysis tool, not only with STED microscopy, but also with SIM measurements. Indeed, SIM-ICCS allows investigating the spatial organization of one nuclear structure, but also the relative distribution of two-color nuclear targets even in the context of crowded samples.

Conclusions and future perspectives

In this thesis, the aim was to develop novel approaches applied to Structured Illumination Microscopy, SIM, for answering specific questions regarding the organization of chromatin in the cell nucleus.

The first developed approach regards an original SIM reconstruction algorithm powered by the Separation of Photons by Lifetime Tuning, SPLIT, method. We demonstrated that SPLIT-SIM is a powerful tool in reconstructing super-resolution, SR, images by exploiting the information 'hidden' in the structured illumination phase shift to separate the sub-diffraction information from the diffraction-limited ones. We showed that this algorithm properly reconstructs SR images without the need of image deconvolution steps, bypassing the traditional "Fourier Reconstruction". We also demonstrated that SPLIT-SIM can be useful in evaluating the quality of the raw data by simply looking at the shape of the phasor plot in case of sparse particles. Eventually, we demonstrated that SPLIT-SIM can be an interesting tool to easily generate SR images of a crowded specimen such as the nuclear environment.

The second approach deals with SIM-ICCS, i.e. SIM coupled with Image Cross-Correlation Spectroscopy, as quantitative step towards the analysis of "multi-color" acquisitions. We tested our microscope and performed two-color analysis on model samples to establish the ground- truth and the capabilities of our pixel-based approach, SIM-ICCS, compared to an object-based method. Then, we demonstrated the appropriateness of the SIM-ICCS in the colocalization analysis to biological imaging of the nuclear environment. Since we aim to investigate oncogene-induced alteration in chromatin organization, we used model cell lines in which it is possible to selectively activate an oncogene to simulate, in vitro, the relative pathology. We started this investigation by performing positive and negative control immunostainings, colocalizing and non-colocalizing targets respectively and then we analyzed them both with SIM-ICCS and with an object-based method.

This is an important step forward within the biophysical objective of studying structure and function relationships in living cells under physiological conditions.

In the future, we will activate specific oncogenes, to verify whether transcription-replication collisions occur in the activated samples, thus confirming the alterations in chromatin organization. To perform such measurements, we plan to gather all the knowledge of this thesis to perform SPLIT-SIM reconstructions of multi-color nuclear images and to analyze them by SIM-ICCS. We also plan to exploit the local analysis of SIM-ICCS to investigate the colocalization of nuclear structures such as replication and transcription machineries.

Overall, each technique presented in this work aims to power SIM to access information about the modifications of the nuclear environment upon activation of oncogenes. We strongly believe that the SIM super resolved approach to image formation in fluorescence microscopy will play a key role in generating new information about the delicate relationship between chromatin structure and its function linked to the development of oncological and neurodegenerative pathologies.

List of Publications

Articles

1. M. Oneto, L. Scipioni, M. J Sarmento, **I. Cainero**, S. Pelicci, L. Furia, P.G. Pelicci, G. I. Dellino, P. Bianchini, M. Faretta, E. Gratton,A. Diaspro, L.Lanzano. (**2019**). "*Nanoscale distribution of nuclear sites analyzed by superresolution STED-ICCS*". Biophysical Journal 117, (11), 2054-2065.

2. **I. Cainero**, E. Cerutti, M. Faretta, G.I. Dellino, P.G. Pelicci, P. Bianchini; G. Vicidomini, A. Diaspro, L. Lanzanò." *Chromatin investigation in the nucleus using structured illumination microscopy powered by SPLIT.*" Submitted to the Biophysical Journal on December 10th.

3. **I. Cainero** et al. "*Measuring nanoscale distances by multicolor structured illumination microscopy*". (in preparation)

Book chapter

Springer Handbook of microscopy. P. Hawkes, J. Spence. (2019) Chapter 21 "*Fluorescence Microscopy*", pages 1039-1088. A.Diaspro, P. Bianchini, F. Cella Zanacchi, L. Lanzanò, G. Vicidomini, M. Oneto, L. Pesce, **I. Cainero**. https://www.springer.com/gp/book/9783030000684

Conference Proceedings

1. **I. Cainero**, M. Oneto, L. Pesce, G. Zanini, L. Lanzanò, A. Diaspro, P. Bianchini (**2017**). "*Combining Expansion Microscopy and STED Nanoscopy for the Study of Cellular Organization*". Biophysical Journal 112 (3), 140a. https://doi.org/10.1016/j.bpj.2016.11.775

2. A. Diaspro, **I. Cainero**, L. Lanzanò, P. Bianchini, G. Vicidomini, F. Cella Zanacchi, L. Pesce, S. Pelicci, M. Oneto, M. Di Bona, M. Faretta, P.Barboro, A. Le Gratiet. (**2018**). "*A Liquid Tunable Microscope as a New*

Paradigm in Optical Microscopy to Paint 4D Chromatin Organisation in the Cell Nucleus". Biophysical Journal 116 (3) 347a.

3. A. Diaspro, N. Anthony, P. Bianchini, **I. Cainero**, M. Di Bona, L. Lanzanò, A. Le Gratiet, R. Marongiu, M. (**2018**). "*LIQUITOPY®: A Liquid Tunable Microscope to Study Chromatin Organization in the Cell Nucleus"*. *Microscopy and Microanalysis* 24 (S1), 1368- 1369. https://doi.org/10.1017/S1431927618007328

4. **I. Cainero**, S. Pelicci, M. Di Bona, A. Diaspro, L.Lanzano. (**2019**). "*A Novel Viewpoint to Analyze Structured Illumination Microscopy (Sim) Data*". Biophysical Journal 116 (3) 280a. https://doi.org/10.1016/j.bpj.2018.11.2361

5. L. Lanzano, M. Oneto, **I. Cainero**, S. Pelicci, M. Sarmento, L. Scipioni, M. Faretta, L. Furia, G. I. Dellino, P. G. Pelicci, P. Bianchini, A. Diaspro. (**2019**). "*Chromatin Alterations in a Model of Oncogene Activation Studied by Advanced Fluorescence Microscopy*" (2019). *Biophysical Journal* 116 (3), 280a.

6. M. Di Bona, S. Pelicci, **I. Cainero**, G. Vicidomini, D. Mazza, M. A. Mancini, A. Diaspro (**2019**). Intensity Sorted Fluorescence Correlation Spectroscopy: "*A Novel Method to Probe Nuclear Dynamics and Chromatin Organization in Living Cells*". *Biophysical Journal* 116 (3) 72a. https://doi.org/10.1016/j.bpj.2018.11.429

7. S. Pelicci, M. Oneto, M. Di Bona, **I. Cainero**, P. Barboro, A. Diaspro, L. Lanzano (**2019**). "*Chromatin Nanoscale Organization Investigated by FLIM-FRET and STED Superresolution Microscopy*". *Biophysical Journal* 116 (3), 174a. https://doi.org/10.1016/j.bpj.2018.11.965

8. E. Cerutti, **I. Cainero**, G. I. Dellino, M. Faretta, P. G. Pelicci, A. Diaspro, L. Lanzano. (**2020**). "*An Image-Based Approach to the Evaluation of Oncogene Activation Effects on Cell's Genomic Stability"*. Biophysical Journal 118 (3) 65a.

9. A. Trianni, N. Anthony, **I. Cainero**, A. Diaspro. (2020). "*SIM-Enhanced Ptychography Imaging of Hela Cells"*. Biophysical Journal 118 (3) 312a.

Oral Presentations

1. **I. Cainero**, E. Cerutti , S. Pelicci , M. Faretta , G.I. Dellino , P.G. Pelicci, A. Diaspro, L. Lanzanò. *"Structured Illumination microscopy as a tool to investigate oncogene-induced alterations in chromatin organization."* 64th Biophysical Society Meeting, San Diego (February 15th-19th, 2020).
2. **I. Cainero**, A. Diaspro, L. Lanzanò. *"SPLIT-SIM: an innovative approach to analyze Structured Illumination Microscopy (SIM) data"*. FOM, Osaka (April 5th-9th, 2020). Conference canceled due to Covid-19 Pandemic.

Poster Presentations

1. **I. Cainero**, M. Oneto, L. Pesce, G. Zanini, L. Lanzanò, A. Diaspro, P. Bianchini (**2017**). "*Combining Expansion Microscopy and STED Nanoscopy for the Study of Cellular Organization*". Biophysical Journal 112 (3), 140°. https://doi.org/10.1016/j.bpj.2016.11.775

2. **I. Cainero**, A.Le Gratiet, P.Bianchini, L.Lanzanò, A.Diaspro(**2018**). "*Combining Structured Illumination Microscopy (SIM) and Separation of Photons by Lifetime Tuning (SPLIT) in a multimodal imaging architecture to study in-situ chromatin organization*". Biophysical Society Meeting, Late Abstract (18-L- 5613-BPS)

3. **I. Cainero**, S. Pelicci, M. Di Bona, A. Diaspro, L. Lanzano. (**2019**). "*A Novel Viewpoint to Analyze Structured Illumination Microscopy (Sim) Data*". Biophysical Journal 116 (3) 280a. https://doi.org/10.1016/j.bpj.2018.11.2361

4. **I. Cainero,** E. Cerutti, A. Diaspro, L. Lanzanò. (**2020**) **"***IMAGE reconstruction in structured illumination microscopy (SIM) by SPLIT- SIM".* 106° Congresso della Società Italiana di Fisica, (September 14th-18th, 2020)

Bibliography

1. Flemming, W. Zellsubstanz, Kern und Zelltheilung. F. C. W. Vogel; Leipzig: 1882.
2. Dutnall and Ramakrishnan 1997)
3. Luger, K.; Mäder, A.W.; Richmond, R.K.; Sargent, D.F.; Richmond, T.J. Crystal structure of the nucleosome core particle at 2.8 A resolution. *Nature* 1997, *389*, 251–260. [CrossRef] [PubMed]
4. Hergeth, S.P.; Schneider, R. The H1 linker histones: Multifunctional proteins beyond the nucleosomal core particle. *EMBO Rep.* 2015, *16*, 1439–1453.
5. Bednar, J.; Garcia-Saez, I.; Boopathi, R.; Cutter, A.R.; Papai, G.; Reymer, A.; Syed, S.H.; Lone, I.N.; Tonchev, O.; Crucifix, C.; et al. Structure and Dynamics of a 197 bp Nucleosome in Complex with Linker Histone H1. *Mol. Cell* 2017, *66*, 384–397.
6. Felsenfeld G, Groudine M. Controlling the double helix. Nature. 2003; 421:448–453. [PubMed: 12540921]
7. Gerchman SE, Ramakrishnan V. Chromatin higher-order structure studied by neutron scattering and scanning transmission electron microscopy. Proc Natl Acad Sci U S A. 1987; 84:7802–7806. [PubMed: 3479765]
8. Maeshima K, Hihara S, Eltsov M. Chromatin structure: does the 30-nm fibre exist in vivo? Curr Opin Cell Biol. 2010; 22:291–297. [PubMed: 20346642]
9. Lawrence, M.; Daujat, S.; Schneider, R. Lateral Thinking: How Histone Modifications Regulate Gene Expression. *Trends Genet.* 2016, *32*, 42–56.
10. Tropberger, P.; Schneider, R. Scratching the (lateral) surface of chromatin regulation by histone modifications. *Nat. Struct. Mol. Biol.* 2013, *20*, 657–661.
11. Vaquerizas, J.M.; Torres-Padilla, M.-E. Developmental biology: Panoramic views of the early epigenome. *Nature* 2016, *537*, 494–496.
12. Shen S., Bonnefil P.C. Post translational modification of histones in oligodendrocyte lineage cellsin development and disease. *J Mol Neurosci*. 2008 May; 35(1): 13–22.
13. El Kennani S. et al. Proteomic Analysis of Histone Variants and Their PTMs: Strategies and Pitfalls. Proteomes. 2018 Sep; 6(3): 29.
14. Cubenas-Potts C., Corces V.G. Architectural proteins, transcription, and the three-dimensional organization of the Genome. FEBS Lett. 2015 Oct 7; 589(20 0 0): 2923–2930.
15. Misteli, T., et al. (2007) Beyond the Sequence: Cellular Organization of Genome Function. *Cell*, 128 (4), 787–800.

16. Cremer, T., and Cremer, C. (2001) Chromosome territories, nuclear architecture and gene regulation in mammalian cells. *Nat. Rev. Genet.*, 2 (4), 292–301.
17. Trojer, P., and Reinberg, D. (2007) Facultative Heterochromatin: Is There a Distinctive Molecular Signature? *Mol. Cell*, 28 (1), 1–13.
18. Lomberk G. et al. The heterochromatin Protein 1 family. Genome Biol. 2006; 7(7): 228.
19. Li, B., Carey, M., and Workman, J.L. (2007) The Role of Chromatin during Transcription. *Cell*, 128 (4), 707–719.
20. MacAlpine, D.M., and Almouzni, G. (2013) Chromatin and DNA Replication. *Cold Spring Harb. Perspect. Biol.*
21. Misteli, T. (2010) Higher-order genome organization in human disease. *Cold Spring Harb. Perspect. Biol.*, 2 (8), a000794–a000794
22. Dellino G.I., Pelicci P.G. *et al*." Next-generation sequencing and DNA replication in human cells: the future has arrived". *Future Oncol*, 10 (2014), pp. 683-693
23. Wey X., *et al*. "Segregation of transcription and replication sites into higher order domains". *Science*, 281 (1998), pp. 1502-1506
24. Trzaskoma, P., Ruszczycki, B., Lee, B. *et al.* Ultrastructural visualization of 3D chromatin folding using volume electron microscopy and DNA in situ hybridization. *Nat Commun* 11, 2120 (2020)
25. Derenzini M, Viron A, Puvion-Dutilleul F. The Feulgen-like osmium-ammine reaction as a tool to investigate chromatin structure in thin sections. J Ultrastruct Res. 1982;80:133-47
26. Derenzini M, Olins AL, Olins DE. Chromatin structure in situ: the contribution of DNA ultrastructural cytochemistry. *Eur J Histochem*. 2014;58(1):2307. Published 2014 Jan 24. doi:10.4081/ejh.2014.2307
27. Robinson, P.J.J., Fairall, L., Huynh, V.A.T., and Rhodes, D. (2006) EM measurements define the dimensions of the "30-nm" chromatin fiber: Evidence for a compact, interdigitated structure. *Proc. Natl. Acad. Sci.*, 103 (17), 6506 LP – 6511
28. M. Adrian, J. Dubochet, J. Lepault, M.W. Adrian, Cryo-electron microscopy of viruses, Nature 308 (1984) 32–36.
29. Song, F., Chen, P., Sun, D., Wang, M., Dong, L., Liang, D., Xu, R.-M., Zhu, P., and Li, G. (2014) Cryo-EM Study of the Chromatin Fiber Reveals a Double Helix Twisted by Tetranucleosomal Units. *Science (80).*, 344 (6182), 376 LP – 380.
30. Jang S., Song F. (2019). The big picture of chromatin by cryo-EM. Current opinion on structural biologi, 58 (76-87).

31. Wilson M.D., Costa A. Cryo-electron microscopy of Chromatin Biology. Structural Biology (2017)
32. Ou HD, Phan S, Deerinck TJ, Thor A, Ellisman MH, O'Shea CC. ChromEMT: Visualizing 3D chromatin structure and compaction in interphase and mitotic cells. Science. 2017 Jul 28;357(6349): eaag0025. doi: 10.1126/ science. aag0025. PMID: 28751582; PMCID: PMC5646685.
33. Wineya M. et al. Conventional transmission Electron Microscopy. Molecular biology of the cell 25(3):319-323. (2014)
34. Woodcock, C.L., and Horowitz, R.A. (1997) Electron Microscopy of Chromatin. *Methods*, 12 (1), 84–95.
35. Steinbrecht RA, Müller M: Freeze-substitution and freeze-drying. Cryotechniques in biological electron microscopy. Springer, Berlin, pp. 149–72 (1987).
36. Birk UJ. Super-Resolution Microscopy of Chromatin. *Genes (Basel)*. 2019;10(7):493. Published 2019 Jun 28. doi:10.3390/genes10070493
37. Zessin PJ,. Super-resolution fluorescence imaging of chromosomal DNA. J Struct Biol. 2012 Feb;177(2):344-8. doi: 10.1016/j.jsb.2011.12.015. Epub 2011 Dec 29. PMID: 22226957.
38. Ricci M.A., et al. Chromatin Fibers Are Formed by Heterogeneous Groups of Nucleosomes In Vivo. 160, 6, P1145-1158. (2015)
39. Boettiger, A. *et al.* Super-resolution imaging reveals distinct chromatin folding for different epigenetic states. *Nature* 529, 418–422 (2016).
40. Matsuda A, et al. Condensed mitotic chromosome structure at nanometer resolution using PALM and EGFP- histones. PLoS One. 2010 Sep 15;5(9):e12768..
41. Kostiuk G. et al. Application of STED imaging for chromatin studies. Journal of Physics D: Applied Physics, Volume 52, Number 50
42. Schermelleh L. et al. Subdiffraction Multicolor Imaging of the Nuclear Periphery with 3D Structured Illumination Microscopy. *Science.* 320, 5881, pp. 1332-1336 (2008)
43. Smeets D, et al. Three-dimensional super-resolution microscopy of the inactive X chromosome territory reveals a collapse of its active nuclear compartment harboring distinct Xist RNA foci. Epigenetics Chromatin. 2014 Apr 28;7:8. doi: 10.1186/1756-8935-7-8.
44. Lichtman JW, Conchello JA. Fluorescence microscopy. Nat Methods. 2005 Dec;2(12):910-9. doi: 10.1038/nmeth817. PMID: 16299476.
45. Diaspro A. Optical Fluorescence microscopy: from the spectral to the nanodimension. Springer (2011)

46. Combs CA, Shroff H. Fluorescence Microscopy: A Concise Guide to Current Imaging Methods. Curr Protoc Neurosci. 2017 Apr 10;79:2.1.1-2.1.25. doi: 10.1002/cpns.29. PMID: 28398640.
47. Abbe, E. (1873). Theorie des Mikroskops und der mikroskopischen Wahrnehmung. *Archiv fur mikroskopische Anatomie*, 413-418. doi:10.1007/BF02956173
48. Pawley, J.B. (2006) Handbook Of Biological Confocal Microscopy. *Springerscience+bus. Media*, third edit.
49. Diaspro, A., Faretta, M., and Sapuppo, P. (2008) *Confocal Microscopy*, Leica Microsystems.
50. Diaspro A. Circumventing the diffraction barrier.Il nuovo saggiatore (2014)
51. Sheppard C.J.R. Fundamentals of superresolution. Micron,38,2, 165-169 (2007)
52. Hess ST, Girirajan TP, Mason MD. Ultra-high resolution imaging by fluorescence photoactivation localization microscopy. *Biophys J*. 2006;91(11):4258-4272. doi:10.1529/biophysj.106.091116
53. Betzig E., et al. Imaging intracellular fluorescent proteins at nanometer resolution. *Science*. 1642-1645. (2006)
54. Stefan W. Hell and Jan Wichmann, "Breaking the diffraction resolution limit by stimulated emission: stimulated-emission-depletion fluorescence microscopy," Opt. Lett. 19, 780-782 (1994)
55. Gustafsson M.G.L. Surpassing the lateral resolution limit by a factor of two using structured illumination microscopy. Journal of Microscopy. (2001)
56. Huang B, Wang W, Bates M, Zhuang X. Three-dimensional super-resolution imaging by stochastic optical reconstruction microscopy. *Science*. 2008;319(5864):810-813. doi:10.1126/science.1153529
57. Prakash, K., Fournier, D., Redl, S., Best, G., Borsos, M., Tiwari, V.K., Tachibana-Konwalski, K., Ketting, R.F., Parekh, S.H., Cremer, C., and Birk, U.J. (2015) Superresolution imaging reveals structurally distinct periodic patterns of chromatin along pachytene chromosomes. *Proc. Natl. Acad. Sci. U. S. A.*, 112 (47), 14635–14640.
58. Nozaki, T., Imai, R., Tanbo, M., Nagashima, R., Tamura, S., and Tani, T. (2017) Dynamic Organization of Chromatin Domains Revealed by Super- Resolution Live-Cell Imaging Article Dynamic Organization of Chromatin Domains Revealed by Super-Resolution Live-Cell Imaging. *Mol. Cell*, 67 (2), 282-293.e7.
59. Lanzanò, L., Coto Hernández, I., Castello, M. *et al.* Encoding and decoding spatio-temporal information for super-resolution microscopy. *Nat Commun* **6,** 6701 (2015).

60. Sarmento, M.J., Oneto, M., Pelicci, S. *et al.* Exploiting the tunability of stimulated emission depletion microscopy for super-resolution imaging of nuclear structures. *Nat Commun* **9,** 3415 (2018).
61. Reindl, J., Girst, S., Walsh, D.W.M., Greubel, C., Schwarz, B., Siebenwirth, C., Drexler, G.A., Friedl, A.A., and Dollinger, G. (2017) Chromatin organization revealed by nanostructure of irradiation induced γH2AX, 53BP1 and Rad51 foci. *Sci. Rep.*, 7 (1), 40616.
62. Cseresnyes, Z., Schwarz, U., and Green, C.M. (2009) Analysis of replication factories in human cells by super-resolution light microscopy. *BMC Cell Biol*, 12, 1–12.
63. Kostiuk, G., Bucevičius, J., Gerasimaitė, R., and Lukinavičius, G. (2019) Application of STED imaging for chromatin studies. *J. Phys. D. Appl. Phys.*, 52 (50), 504003.
64. Gustafsson MG, Shao L, Carlton PM, et al. Three-dimensional resolution doubling in wide-field fluorescence microscopy by structured illumination. *Biophys J*. 2008;94(12):4957-4970. doi:10.1529/biophysj.107.120345
65. Wu Y. & Schroff H. Faster, Sharper and deeper: structured illumination microscopy for biological imaging.Nat. Methods 15, 1011-1019 (2018)
66. Heintzmann R. & Huser T. Super-resolution structured illumination microscopy. Chem. Rev. 117, 13890-13908 (2017)
67. Sheppard C.J.R. Super-resolution in confocal imaging. Optik (Stuttg)80, 53-54 (1988).
68. Muller C.B. & Enderlein. Image scanning microscopy. Phys. Rev. Lett. 104,198101 (2010)
69. York A.G. et al. Resolution doubling in live, multicellular orfanisms via multifocal structured illumination microscopy. Nat. Methods 9,749-754 (2012)
70. Schultz o., et al. Resolution doubling in fluorescence microscopy with confocal spinning-disk image scanning microscopy. Proc- Natl.Acad.Sci. USA 110,21000-21005 (2013).
71. Schermelleh L, Ferrand A, Huser T, Eggeling C, Sauer M, Biehlmaier O, Drummen GPC. Super-resolution microscopy demystified. Nat Cell Biol. 2019 Jan;21(1):72-84. doi: 10.1038/s41556-018-0251-8. Epub 2019 Jan 2. PMID: 30602772.
72. Dammerle J. et al. Strategic and practical guidelines for successful structured illumination microscopy. Nat. Proc. 12, 988-1010 (2017)
73. Rossberger S. et al. Combination of Structured Illumination and single molecule localization microscopy in one setup. J. Opt. 15, (9) (2013).

74. Monkemoller V. et al. Multimodal super-resolution optical microscopy visualizes the close connection between membrane and the cytoskeleton in liver sinusoidal endothelial cell fenestrations. Sci. Rep. 5, 16279 (2015).
75. Hesper Rego E., et al. Nonlinear structured-illumination microscopy with a photoswitchable protein reveals cellular structures at 50-nm resolution. Proc. Nat. Acad. Sci. 109 (3) E135-E143. (2012)
76. Gustafsson M.G.L. Non-linear structured illumination microscopy: Wide-field fluorescence imaging with theoretically unlimited resolution. Proc. Natl. Acad. Sci. USA 102 (37) 13081-13086. (2005)
77. Li D. et al. Extended-resolution structured illumination imaging of endocytic and cytoskeletal dynamics. Science. 349 (6251), aab3500.
78. Schermelleh L. et al. Subdiffraction multicolor imaging of the nuclear periphery with 3D structured illumination microscopy. Science, 320 (5881) 1332-1336. (2008)
79. Wang C. J. R. et al. Interlock formation and coiling of meiotic chromosomes axes during synapsis. Genetics 183 (3), 905-915. (2009).
80. Sonnen K.F., et al. 3D- structured illumination microscopy provides novel insights into architecture of human centrosomes. Biol. Open, 1 (10), 965-976. (2012).
81. Markaki, Y., et al. The potential of 3D-FISH and super-resolution structured illumination microscopy for studies of 3D nuclear architecture. *BioEssays*, 34 (5), 412–426. (2012)
82. Chagin V.O. et al. 4D visualization of replication foci in mammalioan cells corresponding to individual replicons. Nat. Commun. 7, 11231 (2016).
83. Bisson-Filho A.W., et al. Treadmilling by FtsZ filaments drives peptidoglycan synthesis and bacterial cell division. Science, 355 (6326), 739-743. (2017)
84. Regev-Rudzi N., et al. Cell-cell communication between malaria-infected red blood cells via exosome-like vesicles. Cell. 153 (5), 1120-1133. (2013)
85. Rowlett V.W. & Margolin W. 3D-SIM super-resolution of FtsZ and its membrane tethers in Escherichia coli cells. Biophys. J. 107 (8), L17-L20. (2014)
86. Tilsner J., et al. Replication and trafficking of plant virus are coupled at the entrances of plasmodesmata. J. Cell. Biol. 201 (7) 981-995. (2013)
87. Riglar D., et al. Spatial association with PTEX complexes defines regions for effector export into Plasmodium falciparum-infected erythrocytes. Nat. Commun. 4, 1415. (2013)
88. Lesterlin C., et al.RecA boundles mediate gomology pairing between distant sisters during DNA break repair. Nature. 506 (7487, 249-253. (2014)

89. Horsington J., et al. Sub-viral imaging of vaccinia virus using super-resolution microscopy. J. virol. Methods. 186 (1-2), 132-136 (2012).
90. Fitzgibbon J., et al. Super-resolution imaging of plasmodesmata using three-dimensional structured illumination microscopy. Plant. Fisiol. 153 (4), 1453-1463. (2010)
91. Görisch, S.M.; Wachsmuth, M.; Tóth, K.F.; Lichter, P.; Rippe, K. Histone acetylation increases chromatin accessibility. J. Cell. Sci. 2005, 118, 5825–5834.
92. Nagashima, R.; Hibino, K.; Ashwin, S.S.; Babokhov, M.; Fujishiro, S.; Imai, R.; Nozaki, T.; Tamura, S.; Tani, T.; Kimura, H.; et al. Single nucleosome imaging reveals loose genome chromatin networks via active RNA polymerase II. J. Cell Biol. 2019, 218, 1511–1530.
93. Shopland, L.S.; Lynch, C.R.; Peterson, K.A.; Thornton, K.; Kepper, N.; Hase, J. von; Stein, S.; Vincent, S.; Molloy, K.R.; Kreth, G.; et al. Folding and organization of a contiguous chromosome region according to the gene distribution pattern in primary genomic sequence. J. Cell Biol. 2006, 174, 27–38.
94. Spöri, U.; Failla, A.V.; Cremer, C. Superresolution size determination in fluorescence microscopy: A comparison between spatially modulated illumination and confocal laser scanning microscopy. J. Appl. Phys. 2004, 95, 8436–8443.
95. Cremer, C.; Birk, U. Perspectives in super-resolved fluorescence microscopy: What comes next? Front. Phys. 2016, 4, 11.
96. Chapman, J.R.; Sossick, A.J.; Boulton, S.J.; Jackson, S.P. BRCA1-associated exclusion of 53BP1 from DNA damage sites underlies temporal control of DNA repair. J. Cell. Sci. 2012, 125, 3529–3534.
97. Wanner, G., Schroeder-Reiter, E., Ma, W., Houben, A., and Schubert, V. (2015) The ultrastructure of mono- and holocentric plant centromeres: an immunological investigation by structured illumination microscopy and scanning electron microscopy. *Chromosoma*, 124 (4), 503–517.
98. Fišerová J. Et al. Chromatin organization at the nuclear periphery as revealed by image analysis of structured illumination microscopy data. Journal of Cell Science (2017) 130: 2066-2077
99. Hansen, A.S.; Pustova, I.; Cattoglio, C.; Tjian, R.; Darzacq, X. CTCF and cohesin regulate chromatin loop stability with distinct dynamics. eLife 2017, 6.
100. Szalaj, P., Plewczynski, D. Three-dimensional organization and dynamics of the genome.*Cell Biol Toxicol* 34, 381–404 (2018).
101. Ball G, Demmerle J, Kaufmann R, Davis I, Dobbie IM, Schermelleh L. SIMcheck: a Toolbox for Successful Super-resolution Structured Illumination Microscopy. *Sci Rep* 5, 15915 (2015).

102. Lal A, Shan C, Xi P. Structured Illumination Microscopy Image Reconstruction Algorithm. *IEEE Journal of Selected Topics in Quantum Electronics* 22, 50-63 (2016).
103. Huang X*, et al.* Fast, long-term, super-resolution imaging with Hessian structured illumination microscopy. *Nature biotechnology* 36, 451-459 (2018).
104. Wicker K, Mandula O, Best G, Fiolka R, Heintzmann R. Phase optimisation for structured illumination microscopy. *Opt Express* 21, 2032-2049 (2013).
105. Muller M, Monkemoller V, Hennig S, Hubner W, Huser T. Open-source image reconstruction of super-resolution structured illumination microscopy data in ImageJ. *Nat Commun* 7, 10980 (2016).
106. Krizek P, Lukes T, Ovesny M, Fliegel K, Hagen GM. SIMToolbox: a MATLAB toolbox for structured illumination fluorescence microscopy. *Bioinformatics* 32, 318-320 (2016).
107. Oneto M*, et al.* Nanoscale Distribution of Nuclear Sites by Super-Resolved Image Cross-Correlation Spectroscopy. *Biophys J* 117, 2054-2065 (2019).
108. Schneider CA, Rasband WS, Eliceiri KW. NIH Image to ImageJ: 25 years of image analysis. *Nature methods* 9, 671-675 (2012).
109. Bolte S, Cordelieres FP. A guided tour into subcellular colocalization analysis in light microscopy. *J Microsc* 224, 213-232 (2006).
110. Choe KN, Moldovan GL. Forging Ahead through Darkness: PCNA, Still the Principal Conductor at the Replication Fork. *Mol Cell* 65, 380-392 (2017).
111. Heintzmann R, Jovin TM, Cremer C. Saturated patterned excitation microscopy--a concept for optical resolution improvement. *J Opt Soc Am A Opt Image Sci Vis* 19, 1599-1609 (2002).
112. Markaki Y*, et al.* Functional nuclear organization of transcription and DNA replication: a topographical marriage between chromatin domains and the interchromatin compartment. *Cold Spring Harb Symp Quant Biol* 75, 475-492 (2010).
113. Markwirth A*, et al.* Video-rate multi-color structured illumination microscopy with simultaneous real-time reconstruction. *Nat Commun* 10, 4315 (2019).
114. Cnossen J*, et al.* Localization microscopy at doubled precision with patterned illumination. *Nature methods* 17, 59-63 (2020).

115. Reymond L*, et al.* SIMPLE: Structured illumination based point localization estimator with enhanced precision. *Opt Express* 27, 24578-24590 (2019).

116. *Gustafsdottir S.M., et al. "Proximity ligation assays for sensitive and specific protein analyses". (2005). Analytical Biochemistry. 345 (1): 2–9*

117. Pelicci S., *et al*. “Chromatin nanoscale compaction in live cells visualized by acceptor-to-donor ratio corrected Förster resonance energy transfer between DNA dyes”. *J. Biophotonics* (2019)

118. Stryer L., Haugland R.P. “Energy Transfer: a spectroscopic ruler”. *PNAS*, 1967 Aug., 58(2), 719-26.

119. Schermelleh L*, et al. “*Super-resolution microscopy demystified”. *Nat Cell Biol* 21, 72-84 (2019)

120. Huang B., *et al*. “Breaking the diffraction barrier: super-resolution imaging of cells”. *Cell* 143, 1047-1058 (2010)

121. E.T. Arena, *et al.* “Quantitating the cell: turning images into numbers with ImageJ”. Wiley Interdiscip. Rev. Dev. Biol, 6 (2017), p. e260

122. Magde, D., E. Elson, and W. W. Webb. 1972. Thermodynamic fluctuations in a reacting system-measurement by fluorescence correlation spectroscopy. Phys. Rev. Lett. 29:705–708.

123. Bacia, K., and P. Schwille. 2007. Practical guidelines for dual-color fluorescence cross-correlation spectroscopy. Nat. Protoc. 2:2842– 2856.

124. Foo, Y. H., N. Naredi-Rainer, ., T. Wohland. 2012. Factors affecting the quantification of biomolecular interactions by fluorescence cross- correlation spectroscopy. Biophys. J. 102:1174–1183.

125. Di Bona, M., M. A. Mancini, ., L. Lanzano`. 2019. Measuring mobility in chromatin by intensity-sorted FCS. Biophys. J. 116:987– 999.

126. Comeau J.W., et al. A guide to accurare fluorescence microscopy colocalization measurements. Biophys. J. 91:4611-4622. (2006)

127. Dreier J. et al. “Superresolution and fluorescence dynamics evidence reveal that intact liposomes do not cross the human skin barrier”. *PLoS One*, 11 (2016), p. e0146514

128. Scipioni L. et al. Phasor Analysis of Local ICS Detects Heterogeneity in Size and Number of Intracellular Vesicles. Biophysical Journal. Volume 111, Issue 3, 9 August 2016, Pages 619-629

129. Dreier J. et al. “**Superresolution and fluorescence dynamics evidence reveal that intact liposomes do not cross the human skin barrier”.** *PLoS One*, 11 (2016), p. e0146514

130. Negrini S, Gorgoulis VG, Halazonetis TD. Genomic instability--an evolving hallmark of cancer. Nature reviews Molecular cell biology. 2010;11:220-8, doi:10.1038/nrm2858.

131. Markaki Y*, et al. "*Functional nuclear organization of transcription and DNA replication: a topographical marriage between chromatin domains and the interchromatin compartment". *Cold Spring Harb Symp Quant Biol* 75, 475-492 (2010).

132. Wey X., *et al*. "Segregation of transcription and replication sites into higher order domains". *Science*, 281 (1998), pp. 1502-1506

133. Gaillard H, Garcia-Muse T, Aguilera A. Replication stress and cancer. Nature reviews Cancer. 2015;15:276-89, doi:10.1038/nrc3916.

134. Kotsantis P, Silva LM, Irmscher S, Jones RM, Folkes L, Gromak N, et al. Increased global transcription activity as a mechanism of replication stress in cancer. Nat Commun. 2016;7:13087, doi:10.1038/ncomms13087.

135. Helmrich A, Ballarino M, Nudler E, Tora L. Transcription-replication encounters, consequences and genomic instability. Nature structural & molecular biology. 2013;20:412-8, doi:10.1038/nsmb.2543.

136. Kantidakis T, Saponaro M, Mitter R, Horswell S, Kranz A, Boeing S, et al. Mutation of cancer driver MLL2 results in transcription stress and genome instability. Genes Dev. 2016;30:408-20, doi:10.1101/gad.275453.115.

137. Jung P, Menssen A, Mayr D, Hermeking H. AP4 encodes a c-MYC-inducible repressor of p21. Proc Natl Acad Sci U S A. 2008 Sep 30;105(39):15046-51. doi: 10.1073/pnas.0801773105. Epub 2008 Sep 25.

138. Miller DM, Thomas SD, Islam A, Muench D, Sedoris K. c-Myc and cancer metabolism. *Clin Cancer Res*. 2012;18(20):5546-5553. doi:10.1158/1078-0432.CCR-12-0977

139. Alexandrow MG, Kawabata M, Aakre M, Moses HL. Overexpression of the c-Myc oncoprotein blocks the growth-inhibitory response but is required for the mitogenic effects of transforming growth factor beta 1. Proc Natl Acad Sci U S A. 1995 Apr 11;92(8):3239-43.

140. Burns JS, Manda G. Metabolic Pathways of the Warburg Effect in Health and Disease: Perspectives of Choice, Chain or Chance. *Int J Mol Sci*. 2017;18(12):2755. Published 2017 Dec 19. doi:10.3390/ijms18122755

141. Grisolano JL, Wesselschmidt RL, Pelicci PG, Ley TJ. Altered myeloid development and acute leukemia in transgenic mice expressing PML-RAR alpha under control of cathepsin G regulatory sequences. Blood. 1997 Jan 15;89(2):376-87.

142. Rogaia D, Grignani F, Grignani F, Nicoletti I, Pelicci PG. The acute promyelocytic leukemia-specific PML/RAR alpha fusion protein reduces the frequency of commitment to apoptosis upon growth factor deprivation of GM-CSF-dependent myeloid cells. Leukemia. 1995 Sep;9(9):1467-72.

143. Grignani, F, Gelmetti, V, Fanelli, M, Rogaia, D, De Matteis, S, Ferrara, F F, Bonci, D, Grignani, F, Nervi, C, and Pelicci, P G. "Formation of PML/RAR Alpha High Molecular Weight Nuclear Complexes through the PML Coiled-coil Region Is Essential for the PML/RAR Alpha-mediated Retinoic Acid Response." *Oncogene* 18.46 (1999): 6313-321.